

ON ITS WAY TO THE NEUTRON STAR – WHITE DWARF BINARY GRAVEYARD, IGR J16194–2810, A FIRST ASCENT M GIANT X-RAY BINARY

KENNETH H. HINKLE,¹ FRANCIS C. FEKEL,² OSCAR STRANIERO,³ ZACHARY G. MAAS,⁴
RICHARD R. JOYCE,¹ THOMAS LEBZELTER,⁵ MATTHEW W. MUTERSPAUGH,⁶ AND JAMES R. SOWELL⁷

¹*NSF's National Optical-Infrared Astronomy Research Laboratory,
P.O. Box 26732, Tucson, AZ 85726, USA*

²*Center of Excellence in Information Systems, Tennessee State University,
3500 John A. Merritt Boulevard, Box 9501, Nashville, TN 37209, USA*

³*INAF, Osservatorio Astronomico d'Abruzzo,
I-64100 Teramo, Italy, and INFN, Sezione di Roma La Sapienza, Roma, Italy*

⁴*Indiana University Bloomington, Astronomy Department,
727 East Third Street, Bloomington, IN 47405, USA*

⁵*Department of Astrophysics, University of Vienna, Türkenschanzstrasse 17, 1180 Vienna, Austria*

⁶*Columbia State Community College, 1665 Hampshire Pike, Columbia, TN 39401, USA*

⁷*School of Physics, Georgia Institute of Technology, Atlanta, GA 30332, USA*

ABSTRACT

A single-lined spectroscopic orbit for the M giant in the X-ray binary IGR J16194–2810 is determined from a time-series of optical spectra. The spectroscopic orbital period of 192.5 days is twice that of the photometric period, confirming that the M giant in the system is an ellipsoidal variable. The giant is identified as a first ascent giant approaching the red giant tip. The primary is a neutron star (NS) with its M giant companion filling its Roche lobe verifying the system classification as a Low-Mass X-ray binary (LMXB). Stellar C, N, O and Fe abundances are derived for the M giant with the C, N, O values typical for a field giant with $[\text{Fe}/\text{H}] = -0.14$. The system does not have a large kick velocity. Models for the evolution of the system into a binary NS – white dwarf (WD) are presented. The X-ray properties are discussed in the context of this model. This binary is a rare example of a luminous, long orbital period, LMXB early in the transient ellipsoidal phase.

Keywords: Stellar abundances (1577) — Neutron stars (1108) — Ellipsoidal variable stars (455) — Low-mass x-ray binary stars (939) — Multiple star evolution (2153) — Symbiotic binary stars (1674)

1. INTRODUCTION

Late-type giants in binary systems with orbits of a few years or less are classified into one or more families of objects. Among the first categories to be identified was the ‘symbiotic’ (SySt) class where an emission line spectrum is combined with a late-type giant spectrum (Merrill & Hubason 1932). While SySt are now known to be systems with mass loss from a giant being accreted by a degenerate secondary, neither the binarity nor the defining mass transfer was understood until decades after the discovery. SySt are now known to be part of a larger overall class of giants with a degenerate companion. Many of the other groups have peculiar abundances evidencing previous mass transfer. The orbital periods typically require evolution through a main sequence (MS) – giant common envelope (CE) stage (Escorza et al. 2020). While many of these systems are detached, there are SySt with Roche lobe overflow (RLO). Low mass RLO systems have ellipsoidal light variations and are members of the sequence E variables, a group of stars identified in surveys due to their period-luminosity relation (Wood et al. 1999).

With the development of X-ray techniques, additional groups of related objects have been identified including the low mass X-ray binaries (LMXBs) and the X-ray symbiotics (SyXBs), both with a NS primary. In addition, SySt with WD primaries are now being found using X-ray surveys with many of these systems lacking the hallmark strong optical emission (Munari 2019). This is similar to the SyXBs where most are optically quiescent systems, having few, if any, optical emission lines. Membership in the SySt group is based on morphology and not evolutionary commonality. For instance, for the SyXB, in addition to a previous CE stage, a supernova (SN) is required to create the NS (Verbunt & van den Heuvel 1995).

Nearly all of the SyXBs were first cataloged as X-ray sources that were then identified with late-type giants, thus LMXBs, and only subsequently classified as SyXBs. The LMXB group consists mainly of slowly evolving NS – MS binaries with systems containing a late-type giant making up a small fraction. In nearly all LMXBs the mass donor star is in RLO (Verbunt 1993). The RLO systems evolve into NS – WD binaries and, in the process, the transfer of angular momentum spins up the NS. Millisecond pulsar NS – WD binaries are astrophysically important, and there is extensive literature (see, for instance, reviews by Bhattacharya & van den Heuvel (1991), Phinney & Kulkarni (1994), and Verbunt & van den Heuvel (1995)).

In this paper we discuss the binary IGR J16194–2810. This star is an excellent example of inclusion in multiple families of binaries. Initially identified as a NS or black hole (BH) X-ray source (Bird et al. 2006; Bassani et al. 2006; Stephen et al. 2006), IGR J16194–2810 was later found to be coincident with an M III star (Masetti et al. 2007), and hence, was a LMXB. From time-series survey photometry, Kiraga (2012) found the M III star to be an ellipsoidal variable. Due to the M III companion to a NS, it has also been included in lists of SyXB (Yungelson et al. 2019). The multiple classifications do not give insight into the significance of this system. It stands out in the various lists of objects because it is ellipsoidal, has a period that is both abnormally short for a SyXB/SySt and unusually long for a LMXB, but does not have a high X-ray luminosity. We have undertaken a program of spectroscopy to explore the nature of this highly unusual binary.

In the following sections we discuss the optical and near-infrared spectroscopy of the binary system IGR J16194–2810. The new observations are reviewed in the next section. In Section 3 we discuss the orbit. Section 4 starts with a discussion of the identification of IGR J16194–2810 as a NS binary followed by a detailed discussion of the properties of the late-type companion, including the space motion, effective temperature, luminosity, and radius. The mass range of the NS is also reviewed. Then in Section 5 we use its ellipsoidal properties to extract limits on the NS and M III masses and binary inclination. In Section 6, the M giant abundance determinations are discussed. Section 7 includes a discussion of the binary evolution of IGR J16194–2810 with a focus on the end product. Comparisons with various related groups of variables are included, as is a new model based on the current parameters of the system. A summary is presented in the Conclusions, Section 8.

2. OBSERVATIONAL DATA

2.1. Near-IR Spectra

The *H* and *K* regions were observed at spectral resolution $R = \lambda/\Delta\lambda$ of ~ 45000 on 2018 April 22 UT with the Immersion Grating Infrared Spectrometer (IGRINS, Park et al. 2014) at the Gemini South 8-meter telescope (GS). Reductions were the same as those employed for other SyXB spectra observed with IGRINS/GS (Hinkle et al. 2019). In brief, the initial reduction was done with the IGRINS pipeline. The output from this process is the echelle orders ratioed to a telluric reference standard. The continuum in each order was then normalized by doing a linear fit to the high points. Polynomial terms in the continuum were removed with the IRAF¹ continuum routine *splot 't'* at low order. The orders were joined by matching the overlap regions between the orders. The velocities of the *K*-band CO first overtone lines were measured, and the average velocity is listed in Table 1.

Nearly a year after the IGRINS observation, an observation of the 2.299 – 2.311 μm region of the *K* band was taken on 2019 March 17 UT with the Phoenix cryogenic echelle spectrograph (Hinkle et al. 1998) on GS. The spectrum has $R \approx 50000$. The spectral orders were extracted from the raw data and wavelength calibrated with standard reduction techniques (Joyce 1992). In late-type stars the spectral region observed is dominated by a series of strong CO 2-0 lines. The stellar velocity was measured by cross correlation of CO laboratory frequencies to the spectrum with the IRAF cross-correlation routine *fxcor* (Fitzpatrick 1993).

¹ Image Reduction and Analysis Facility software distributed by NOAO (now NOIRLab).

The Phoenix spectrum has much less wavelength coverage than the IGRINS spectrum but proved to be a critical observation. Comparison of the IGRINS and Phoenix radial velocities showed a change consistent with orbital motion at the ellipsoidal period of 192.8 days (Kiraga 2012). No changes in the spectrum resulting from late-type stellar variability were apparent. On the basis of this observation, an effort was launched to obtain a spectroscopic orbit of the M III.

2.2. Visual Spectra

A time series of optical high-resolution spectra was obtained at Fairborn Observatory in southeast Arizona with the Tennessee State University 2 m Automatic Spectroscopic Telescope (AST) and fiber-fed echelle spectrograph (Eaton & Williamson 2004, 2007). The detector is a Fairchild 486 CCD that has a 4096×4096 array of $15 \mu\text{m}$ pixels (Fekel et al. 2013). There are 48 echelle orders that range in wavelength from 3800 to 8260 Å. The observations were obtained with a $365 \mu\text{m}$ fiber that produces a resolution of 0.4 \AA or $R \approx 15000$ at 6000 \AA .

With a V magnitude of 12.75 (Kiraga 2012) and a declination of -28° , IGR J16194–2810 is near the limit of observability of the AST. In addition, due to its southern declination, the observing season for IGR J16194–2810 is relatively short. In spite of these difficulties, between 2019 June and 2022 June, 63 useful spectroscopic observations were acquired.

A discussion of velocity measurement for AST spectra can be found in Fekel et al. (2009). While IGR J16194–2810 is grouped with the symbiotic stars, as with a number of other SyXB, the optical spectrum is that of a normal late-type star, i.e., it does not contain conspicuous emission lines or extensive veiling caused by continuum emission. Thus, the reference-star line list that was used for measurement contains 40 lines that are relatively unblended in M giant spectra and range in wavelength from 5000 to 6800 Å. To fit individual line profiles, a rotational broadening function was used (Lacy & Fekel 2011; Fekel & Griffin 2011). With the same reduction technique, unpublished velocities of several IAU radial-velocity standards observed with the 2 m AST have an average velocity difference of -0.6 km s^{-1} when compared to the results of Scarfe (2010). Thus, we have added 0.6 km s^{-1} to each of our AST velocities. Our radial-velocity observations are listed in Table 1.

In high-resolution spectra the IGR J16194–2810 lines are conspicuously broadened. From a dozen spectra with the best signal-to-noise ratios, the rotational broadening fits resulted in a projected rotational velocity, $v \sin i$, of $16 \pm 1 \text{ km s}^{-1}$ where v is the rotational velocity and i is the inclination. The technique used to measure $v \sin i$ is described in Willmarth et al. (2016) and Henry et al. (2022). Spectrum synthesis of the much higher signal-to-noise IR spectra require a projected rotational broadening of 17 km s^{-1} , a value in accord with the optical measurements.

2.3. Photometry

An I -band light curve for IGR J16194–2810 is presented by Kiraga (2012). The photometry, 375 observations, is from the All Sky Automated Survey (ASAS). At the magnitude of IGR J16194–2810, the uncertainty of an individual measurement can be as much as several tenths of a magnitude but is compensated by the large number of observations. IGR J16194–2810 is, in fact, fainter than the cutoff magnitude of the Kiraga (2012) survey. A discussion of the ASAS data, which includes the IGR J16194–2810 photometry, is given by Pojmański & Maciejewski (2004). Briefly, independent instruments equipped with standard V , R , and I filters took simultaneous photometry through five different sized apertures. For IGR J16194–2810 only V and I data are available. The light curve amplitude of IGR J16194–2810 is $\sim 0.11 \text{ mag}$ at I and $\sim 0.14 \text{ mag}$ at V . The V data are shown in the upper panel of Figure 1. Higher precision photometry is available from Gaia but with much less frequent sampling. Gaia RP -band (Jordi et al. 2010) observations are shown in the lower panel of Figure 1.

3. SPECTROSCOPIC ORBIT

Kiraga (2012) proposed an orbital period of 192.8 days for IGR J16194–2810 based on the ASAS photometric observations. From the shape and amplitude of the light curve, Kiraga (2012) assigned IGR J16194–2810 to the ellipsoidal class of variables. For ellipsoidal variables the photometric period is half the orbital period, so for IGR J16194–2810 the photometric period is 96.4 days (Figure 1). Ellipsoidal variations result from the axial elongated shape of the star(s) with the light curve repeating as the long and short sides of the star are seen twice during an orbit (Morris 1985).

To compute the orbit, equal weights were assigned to the lone IGRINS and Phoenix radial velocities as well as each AST velocity. Adopting the 192.8 day period as a starting value, we obtained a preliminary orbital solution with the

computer program BISP (Wolfe et al. 1967), which uses the Wilsing-Russell method (Wilsing 1893; Russell 1902). We next refined those elements with the program SB1 (Barker et al. 1967), which utilizes differential corrections. That solution produced a period of 192.6 ± 0.2 days and an eccentricity of 0.018 ± 0.008 . Given the very small eccentricity, we next obtained a circular orbit solution with the SB1C orbit program (D. Barlow 1998, private communication), which iterates sine/cosine fits by differential corrections. That solution resulted in a period of 192.5 ± 0.2 days. The orbital and photometric periods are the same to within the uncertainty.

In the case of IGR J16194–2810, the precepts of Lucy & Sweeney (1971) for discriminating between an eccentric and a circular orbit indicate that the eccentric orbit is to be preferred. However, the phase distribution of velocities is far from uniform with much of the drop from maximum velocity to minimum velocity missing. Despite this lack of velocities in that part of the orbit, the resulting orbital eccentricity is only 0.018 with a longitude of periastron, ω , of 64.4 ± 20.1 . Lucy & Sweeney (1971) have argued that such an eccentricity value is so small that it is likely statistical in origin and therefore, not significant. Thus, we have chosen to adopt the circular orbit for IGR J16194–2810.

While the eccentricity that we compute is statistically insignificant, improvements in the orbit may ultimately find a very slight eccentricity. Sterne (1941) noted that small eccentricities can result from the elliptical distortion of the stars in ellipsoidal systems. For the ellipsoidal SySt T CrB, Kenyon & Garcia (1986) argued for the reality of small eccentricities. This work has been reviewed and corrected by Belczyński & Mikołajewska (1998). For an orbital eccentricity resulting from ellipsoidal distortions the longitude of periastron, ω , is expected to be 90° or 270° . For T CrB, Kenyon & Garcia (1986) find $\omega = 80^\circ \pm 6^\circ$. In our IGR J16194–2810 orbit, $\omega = 64^\circ$ with a large uncertainty of 20° .

The orbital elements and derived parameters for IGR J16194–2810 are listed in Table 2. In a circular orbit the element T , a time of periastron passage, is indeterminate. So, as recommended by Batten et al. (1989), T_0 , a time of maximum radial velocity is given instead. A phase plot of the radial velocities compared with the computed orbital curve is shown in Figure 2, where phase zero is a time of maximum velocity.

4. STELLAR PARAMETERS

Since IGR J16194–2810 is an ellipsoidal variable, the stellar parameters can be derived in a variety of ways. In the following subsections we discuss the various inputs and resulting values. The parameters derived are summarized in Table 3.

4.1. Identification and Spectral Type

The X-ray source IGR J16194–2810 was first detected in X-rays above 20 keV by *INTEGRAL/IBIS*² (Bassani et al. 2006; Bird et al. 2006). Stephen et al. (2006) identified that source with *ROSAT*³ 1RXS J161933.6–280726 and with a $B \sim 14$ mag optical counterpart. No pulsations have been detected in the X-ray flux (Enoto et al. 2014). Additional directed observations by Masetti et al. (2007) from *Swift/XRT*⁴ improved the coordinates clearly identifying the M2 III star, 2MASS 16193334–2807397, as the optical source. As a result, IGR J16194–2810 is a member of the LMXB class.

Ratti et al. (2010) confirmed the identification using *Chandra*. A NS in the IGR J16194–2810 binary, originally proposed by Ratti et al. (2010), was supported by Kitamura et al. (2014). They found that the hard X-ray emission originates in a small, 0.7 km, radius on the NS surface with the soft emission possibly from the accretion stream. In addition, the X-ray flux and hardness confirm the NS nature of the degenerate in the IGR J16194–2810 system. The X-ray luminosity is more than 100 times the luminosity of typical WD SySt (Luna et al. 2013).

The 3850–7200 Å region of the spectrum, observed at $R \sim 1000$, is shown in Figure 2 of Masetti et al. (2007). The spectral type assigned, M2 III, is based largely on the near-IR TiO bands. The conspicuous presence of TiO in the spectrum requires that the giant be of type M (Morgan et al. 1943; Abt et al. 1968). Pecaut & Mamajek (2016) independently found a spectral type M2 III based on a different data set. The optical spectrum of IGR J16194–2810 does not contain emission lines, which are a hallmark of traditional SySt systems.

The IGRINS spectrum covers the K and H bands. The spectrum was convolved to $R=3000$ for use in spectral typing. The K – and H –spectra are shown in Figures 3 and 4 along with M giant standard star spectra (Wallace &

² INTErnational Gamma-Ray Astrophysics Laboratory/Imager on Board the INTEGRAL Satellite

³ ROentgen SATellite

⁴ *Swift*/X-Ray Telescope

Hinkle 1997; Meyer et al. 1998). Visual comparison confirms that the near-IR spectrum of IGR J16194–2810 is that of a normal, early M III star but provides no refinement of the spectral type.

4.2. Distance and Space Motion

The Gaia data release 3 (DR3) parallax for IGR J16194–2810 is 0.452 ± 0.036 mas, corresponding to a distance of 2101_{-150}^{+129} pc (Bailer-Jones et al. 2021). Previous distance estimates from extinction and X-ray properties were in the range 3.0 – 3.7 kpc (Ratti et al. 2010; Masetti et al. 2007). The X-ray luminosity (L_X) corrected to 2.1 kpc, 2×10^{35} ergs s^{-1} , is similar to that of other SyXB (Masetti et al. 2007).

Ratti et al. (2010) found a proper motion of 1.3 ± 4.7 mas yr^{-1} in right ascension and -20.2 ± 4.7 mas yr^{-1} in declination and concluded that IGR J16194–2810 has a minimum peculiar velocity of 280 ± 66 km s^{-1} , suggesting a kick velocity. The Gaia proper motion, -0.894 ± 0.043 mas yr^{-1} in right ascension and -5.287 ± 0.027 mas yr^{-1} in declination (Gaia Collaboration 2022), is quite different, as well as two orders of magnitude more accurate.

Using a beam size of circular radius 20 arcmin centered on the position of IGR J16194–2810, sources in the Gaia DR3 archive with parallaxes between 0.35 and 0.65 mas and having a parallax error ≤ 0.045 mas were selected. This results in a total of 98 stars. Histograms of the proper motion of these sources are shown in Figure 5. In this selection of DR3 data, 42 sources also have measured radial velocities, and a histogram of those velocities is also in Figure 5. The arrows mark the values for IGR J16194–2810. The Gaia data shows that IGR J16194–2810 does not have a significant kick velocity. With the assumption that the parallax and proper motion uncertainties are independent, the transverse velocity is -8.9 ± 1.0 km s^{-1} in right ascension and $-52.7_{-3.5}^{+4.0}$ km s^{-1} in declination. The systemic (γ) radial velocity of the binary is -4.36 ± 0.13 km s^{-1} (Table 2). These results produce a space velocity of -57.7 km s^{-1} . This value appears typical for stars in this region of the Milky Way (Figure 5).

4.3. Effective Temperature, Luminosity, Radius

Multiple techniques are available for determining the effective temperature. We employ two, one based on optical/near-IR spectroscopy and the other on infrared photometry. As mentioned in Section 4.1, optical spectra of IGR J16194–2810 are classified as spectral type M2 III based on TiO bands in the red. The effective temperature for a M2 III is ~ 3700 K (Dyck et al. 1996; Van Belle et al. 1999). It is difficult to set an uncertainty on this value due to uncertainty in the spectral classification itself, uncertainty in the spectral types of the reference spectra, and the known scatter in the calibration of effective temperature against other parameters (e.g., see Ramírez et al. 1997).

A more quantified approach is possible with the use of spectral indices. Several authors have calibrated spectral indices in medium resolution K - and H -band spectra. With the use of empirical relations, the indices can be converted to effective temperatures with uncertainties. Ramírez et al. (1997) discuss three K -band indices, a Na blend at $4524 - 4535$ cm^{-1} , a Ca blend at $4409 - 4426$ cm^{-1} , and the ^{12}CO 2-0 bandhead from $4344 - 4362$ cm^{-1} . We measured the equivalent widths of the indices in Wallace & Hinkle (1997) K4 III to M4 III standard spectra and the IGRINS IGR J16194–2810 K -band spectrum convolved to $R=3000$ (Figure 3). The continuum points of the spectra were normalized. Our measurements of the Ca and Na indices in the M III standard spectra have considerable scatter and are not useful for early M stars. Ramírez et al. (1997) found a similar result. However, also as found by Ramírez et al. (1997), the CO index proved to be robust. Calibrating to the standard star equivalent widths listed in Ramírez et al. (1997), the 2-0 ^{12}CO bandhead index for IGR J16194–2810 has an equivalent width of 3.79 ± 0.10 cm^{-1} , 20.0 ± 0.5 Å, with its uncertainty mainly from the continuum placement. Combining uncertainties from the T_{eff} calibration and measurement, $T_{eff} = 3660 \pm 190$ K.

To utilize the spectral indices in the H -band, the high-resolution IGRINS spectrum was convolved to $R = 3000$ and normalized to the continuum of the reference standard star spectra. The spectral indices of Meyer et al. (1998) are marked on Figure 4. Three indices were recommended by Meyer et al. (1998) for measuring the effective temperature of cool stars. The OH 5920 cm^{-1} index has an equivalent width of 1.01 ± 0.10 cm^{-1} and that of the Mg I 6345 cm^{-1} index is 1.96 ± 0.10 cm^{-1} . For early M giants the values of these indices are relatively small and sensitive to the continuum value, and, as a result, the uncertainty is large. From expression 6 of Meyer et al. (1998) $T_{eff} = 3690 \pm 430$ K. As in the K -band, the H -band CO index is more robust. The CO 6170 cm^{-1} index has an equivalent width of 3.65 ± 0.26 cm^{-1} , corresponding to $T_{eff} = 3660$ K. An index – effective temperature relationship with uncertainties is not provided by Meyer et al. (1998). Based on the measurement uncertainty and the scatter in values for the standards, the total uncertainty is $\gtrsim \pm 200$ K.

We next discuss two methods for determining the effective temperature using photometry. A catalog of effective temperatures for symbiotic stars based on fits to the 1 to 15 μm spectral energy distributions (SEDs) was produced by

Akras et al. (2019). The T_{eff} for IGR J16194–2810 is 3779 ± 152 K. However, the effective temperature depends on the reddening and Akras et al. (2019) did not take reddening into account. We independently applied blackbody fitting to the same archival photometry and found an ambiguity between a ~ 3700 K fit with no reddening and a marginally better fits at higher temperatures with enhanced reddening, in particular 4000 K with $A_V = 2.6$ mag. The catalog associated with Akras et al. (2019) also gives a Gaia effective temperature of 3511 K. The colors for IGR J16194–2810 fall outside the color calibration for Gaia so this effective temperature is based on an extrapolation and is not valid.

To determine the reddening, the DUST database⁵ was used to estimate the ISM contribution to the reddening. This indicates $A_V = 1.61$ mag (Green et al. 2018, 2019), corresponding to $A_K = 0.19$ mag. Additional reddening due to circumbinary dust is possible but difficult to estimate. For IGR J16194–2810 the VizieR⁶ catalog lists $K_s = 6.97$ mag and Johnson K and $J = 6.99$ mag and 8.268 mag, respectively. With the use of standard reddening relations (Rieke & Lebofsky 1985) and interstellar reddening with $A_V = 1.61$ mag, $K_0 = 6.79$ mag and $J_0 - K_0 = 1.01$ mag. In the case of additional circumbinary reddening, assuming $A_V = 2.6$ mag, $K_0 = 6.60$ mag and $J_0 - K_0 = 0.84$ mag.

Various color-color indices can be used to derive the effective temperature. Assuming ISM reddening, the $J_0 - K_0$ corresponds to $T_{eff} \sim 3700$ K from the calibration of Tokunaga (2000). Similarly, the closest matching $J - K$ in the Worthey & Lee (2011) models of synthetic photometry are for a $\log(g) = 0.5$ and $[\text{Fe}/\text{H}] = 0$ model and an effective temperature of 3735 K. For $\log(g) = 1$, $T_{eff} = 3672$ K. Using the Houdashelt et al. (2000) models, the color matches $T_{eff} = 3700$ K with $\log(g) = 0.0$ and $[\text{Fe}/\text{H}] = +0.25$. With their calibration this corresponds to spectral type M2.6 III. Additional reddening raises the effective temperature. Adopting $J_0 - K_0$ for circumbinary reddening, the effective temperature is ~ 4400 K, typical of an early K giant. Since this is clearly not the case, $A_V = 1.61$ mag is adopted.

The unweighted mean value from all the above approaches is 3700 K. While systematic uncertainties are present, we assume that the uncertainty is largely from measurement uncertainty. In this case, the uncertainty on the mean is ± 100 K. We adopt 3700 ± 100 K for the effective temperature of IGR J16194–2810.

The luminosity can be derived from the Gaia distance of 2101_{-150}^{+129} pc and photometry. Using $(J_0 - K_0) = 1.01$ mag, Bessell & Wood (1984) give a bolometric correction of 2.71 mag. Combining this with the distance modulus of $11.61_{-0.16}^{+0.13}$ mag and the dereddened observed K magnitude, K_0 , of 6.79 mag, the absolute bolometric magnitude is $-2.22_{-0.12}^{+0.17}$. The luminosity is $573_{-79}^{+72} L_\odot$. Using the effective temperature – radius – luminosity relation and $T_{eff} = 3700 \pm 100$ K, the radius is $58 \pm 7 R_\odot$. This is in agreement with the radius for a standard M2 III, $61 \pm 11 R_\odot$ (Table 7 of Van Belle et al. 1999).

4.4. Mass of the NS

Neutron stars have a limited range of mass from near the Chandrasekhar limit to near collapse into a black hole. A commonly made assumption is that a NS has a mass of $1.35 M_\odot$ or $1.4 M_\odot$ (see, for examples, references in the Australia Telescope National Facility (ATNF) Pulsar Catalog⁷). A mass of $\sim 1.35 M_\odot$ corresponds to both the Chandrasekhar limit and a sharp peak in the distribution of pulsar masses. While the mass distribution of the overall population of NS is peaked at $\sim 1.36 M_\odot$, as discussed in (Özel & Freire 2016), the pulsar population can be divided into groups. Double NS pulsar binaries have masses of $1.33 \pm 0.09 M_\odot$. Two peaks have been identified for millisecond pulsars at 1.49 ± 0.19 and $1.54 \pm 0.23 M_\odot$. NS masses determined with reasonable accuracy range over $\sim 1.2 - 2 M_\odot$ (Özel & Freire 2016).

It could be argued that the IGR J16194–2810 NS falls into one of the groups identified by Özel & Freire (2016), for instance, that the evolutionary end stage of IGR J16194–2810 is likely a NS–He WD. Smedley et al. (2014) find that to make the inclinations of known millisecond pulsar NS–He WD systems random, the mass of the NS must be in the range $1.55 - 1.65 M_\odot$. However, this not only assumes an end state for IGR J16194–2810 but also that the system is at the end of the mass transfer phase. We start by assuming a mass for the NS that is in the full range of $1.2 - 2 M_\odot$. More restricted bounds on the NS mass are discussed below.

5. ELLIPSOIDAL VARIATION

A standard approach for determining the properties of ellipsoidal binaries employs a Wilson – Devinney analysis of the light curve to determine the radius of the visible star, the semimajor axis, the inclination, and the mass ratio

⁵ <https://irsa.ipac.caltech.edu/applications/DUST/>; Schlafly & Finkbeiner (2011)

⁶ <https://vizier.cds.unistra.fr/viz-bin/VizieR>; Ochsenbein et al. (2000)

⁷ Manchester et al. (2005); <http://www.atnf.csiro.au/research/pulsar/psrcat>

(Wilson & Devinney 1971). In the case of IGR J16194–2810, these parameters can be solved with the use of the mass function and $v \sin i$ from the line profiles. The light curve provides additional information on limb darkening and gravity darkening coefficients (Morris 1985). Unfortunately, the uncertainty in the current photometry is too large to provide useful information.

5.1. Mass Function and Rotation

The star(s) in ellipsoidal variables are elongated due to Roche lobe filling. While photometry shows that the M2 III in IGR J16194–2810 is clearly elongated, a critical question is how much of the Roche lobe is filled. The light curve amplitude in the I band, 0.11 magnitudes, places IGR J16194–2810 in the group with the largest amplitudes (Soszyński et al. 2004). The discussion continues with the assumption that the red giant is Roche lobe filling.

For Roche lobe filling systems, the ratio of the masses of the stars, q , is a critical parameter. We define

$$q = M_{RG}/M_{NS}$$

where the mass of the M2 III is M_{RG} and the mass of the NS is M_{NS} .

Morris (1985) has shown that a complete solution for the parameters of an ellipsoidal system is possible for systems where the period, projected rotational velocity, light curve amplitude, spectral type, and mass of one of the components is known. Several approaches are possible. In this section we proceed with a graphical solution where the light curve amplitude is not required (Belczyński & Mikołajewska 1998).

The mass function, $f(m)$, derived from our orbital parameters, $0.3337 \pm 0.0062 M_{\odot}$ (Table 2), can be expressed as

$$f(m) = (M_{NS}^3 \sin^3 i)/(M_{RG} + M_{NS})^2.$$

This can be re-written with the use of the mass ratio q as

$$f(m) = (M_{NS} \sin^3 i)/(1 + q)^2.$$

The relation between q and i from the mass function is shown in Figure 6. Curves are shown spanning the range of NS masses, 1.2 – 2.0 M_{\odot} .

For Roche lobe filling systems the stellar radius, R , is a function of q and the semi-major axis, a . The formulae are summarized in Table 2.1 of Warner (1995). Since the NS has a very small radius compared to the giant, the eclipse angle is $\arctan(R/a)$ and can be expressed as a function of q (Belczyński & Mikołajewska 1998). The limiting angle for an eclipse as a function of q is shown in Figure 6. IGR J16194–2810 does not eclipse, and this sets a limit for the inclination as a function of q .

The rotational broadening of the lines is related to the rotational velocity, v , the inclination i , the stellar radius, R , and the rotation period, P , by

$$v \sin i \lesssim (2\pi R \sin i)/P$$

The M2 III fills its Roche lobe and the radius is by definition the Roche radius. Similarly, the rotation period and orbital period are equal (Morris 1985). With Kepler’s third law, the Roche lobe filling stellar radius can be expressed as a function of q and orbital period. This results in a relation between q and $\sin i$, also plotted on Figure 6. The intersection of the relations from the mass function and $v \sin i$ gives q and i . For the mean value of $v \sin i = 16 \text{ km s}^{-1}$, q is in the range 0.7 – 0.9. Over the entire range of possible $v \sin i$, $q = 0.64 - 0.98$. The inclination is the range $i \sim 55 - 70^{\circ}$.

The filling factor, f , for Roche lobes in ellipsoidal systems can be computed from q and i (Nie et al. 2012). Employing the above range of values for q and i and taking $\Delta R = \Delta I/0.87$, where ΔR and ΔI are the amplitudes of the light curve in the R and I bands and $\Delta I = 0.11$, the filling factor f for the M2 III in IGR J16194–2810 is in the range 0.90 – 0.99. This range for f and related analysis by Nie et al. (2012) confirms that the Roche lobe is filled.

5.2. M Giant Mass and Core Mass

Since the M giant fills its Roche lobe, the radius of the Roche lobe is the radius of the M giant. Defining $\Omega_b = 2\pi/P_b$, where P_b is the binary period,

$$\frac{GM_{RG}}{R_L^3} = 10\Omega_b^2$$

where G is the gravitational constant (Phinney & Kulkarni 1994). From the luminosity and effective temperature, the radius of the red giant is $58 \pm 7 R_{\odot}$ (Section 4.3). With this value and a rotation period of 192.5 days, the mass of the M giant is $0.70_{-0.23}^{+0.28}$. The M giant to NS mass ratio can be found from Figure 6. The extreme range of q is 0.64 – 0.98. For the mean projected rotational velocity, 16 km s^{-1} , the range is $q = 0.7 - 0.9$. The range of NS masses resulting from q and the M giant mass are shown in Figure 7. The NS lower mass limit of $1.2 M_{\odot}$ combined with q limits the lower mass of the M giant to $\gtrsim 0.8 M_{\odot}$. Similarly, the upper mass limit for the M giant (Figure 7) limits the maximum mass of the NS to $\lesssim 1.5 M_{\odot}$. The resulting value for the M III mass is $0.91 \pm 0.07 M_{\odot}$ and for the NS $1.35 \pm 0.15 M_{\odot}$. For the $58 \pm 7 R_{\odot}$ M III radius, the volume average surface gravity of the M2 III is $\sim 5 - 11 \text{ cm s}^{-2}$, i.e. $\log(g) \sim 1$.

The luminosity of a red giant branch (RGB) star depends only on the mass of the degenerate core, as shown by the Paczyński relation (Paczynski 1970; Tuchman et al. 1983). For giants of solar metallicity,

$$L = (M_c/0.16)^8.$$

where the luminosity, L , is in L_{\odot} and M_c is the degenerate helium core mass in M_{\odot} (Phinney & Kulkarni 1994). For IGR J16194–2810, $L = 573_{-79}^{+72} L_{\odot}$ so M_c is $0.35 \pm 0.01 M_{\odot}$. Ellipsoidal variables have a period – luminosity relation so there must also be a relation between the orbital period and the core mass. Tauris & Savonije (1999) provide a fit to models relating the core mass to the orbital period. From their equation 20 with population I constants, M_c is $0.35 M_{\odot}$. The Tauris & Savonije (1999) models are in thermal equilibrium. While Roche-lobe filling, IGR J16194–2810 currently does not have an extreme mass loss rate (Section 7.4), with most of the envelope mass of the M III intact (Section 7.1.2), and this criteria should apply. The agreement of the Paczyński and Tauris-Savonije values supports this.

Renzini et al. (1992) found that since the stellar envelope is convective, the radius of the giant is also a function of the degenerate core mass. From Phinney & Kulkarni (1994)

$$R \simeq 1.3 \left(\frac{M_c}{0.16} \right)^5$$

where the radius, R , is in R_{\odot} . Thus the stellar radius and, in RLO, the size of the Roche lobe, can be determined from only the luminosity, albeit with considerable uncertainty. Alternately, the core mass can be found from the radius. The resulting core mass is $0.34 \pm 0.1 M_{\odot}$, consistent with values found above.

6. ABUNDANCES

Information on the age and evolutionary history of the system potentially can be determined from the star’s chemical composition. In addition, in several places in the above discussion, constants have been used appropriate for stars of near-solar metallicity and this should be confirmed. To determine the $[\text{Fe}/\text{H}]$ abundance, we identified Fe I lines that were not significantly blended with other absorption features, located in spectral regions where the continuum was relatively well defined, and were included in the $1.51 - 1.70 \mu\text{m}$ region of the H -band covered by the *APOGEE*⁸ line list (Shetrone et al. 2015). Synthetic spectra were used to measure abundances and identify blends with the MOOG package (Snedden 1973, Version 2019) and MARCS⁹ model atmospheres (Gustafsson et al. 2008). As a starting value, the solar abundances of Asplund et al. (2009) were assumed. A microturbulence value of 2.0 km s^{-1} was used, a typical value for early M giants (Smith & Lambert 1985; Maas & Pilachowski 2021).

Grids of synthetic spectra were created to measure $[\text{Fe}/\text{H}]$ abundances via χ^2 minimization. Atmospheric models were iterated to match the newly derived $[\text{Fe}/\text{H}]$. Similar analysis of the Arcturus spectrum (Hinkle et al. 1995) produced an abundance consistent with the results of Ramírez & Allende Prieto (2011). The standard deviation calculated from the abundances derived for individual Fe I lines was adopted as the statistical $[\text{Fe}/\text{H}]$ uncertainty. Models at $\pm 100 \text{ K}$ in T_{eff} and ± 0.20 in $\log(g)$ were created individually, the new FeI abundance computed, and the difference adopted as the uncertainty. The atmospheric parameter uncertainties were combined in quadrature with the statistical uncertainty and the total uncertainty is quoted for the abundance, $[\text{Fe}/\text{H}] = -0.14 \pm 0.12$

We also sought to determine the C, N, and O abundances using selected spectral lines from the near-IR transitions of CO, CN, and OH. The line lists used were Li et al. (2015) for CO, Brooke et al. (2014) for CN, and Brooke et al.

⁸ Apache Point Observatory Galactic Evolution Experiment

⁹ Model Atmospheres with a Radiative and Convective Scheme

(2016) for OH. Lines from the H -band CO second overtone could not be identified. For CO we selected a list of least blended lines in the K -band first overtone by using the technique discussed in Hinkle et al. (2016). As we did for the $[\text{Fe}/\text{H}]$ analysis, abundances were derived with MOOG spectral synthesis software and MARCS 1D atmospheric models. A MARCS model was selected matching $T_{\text{eff}} = 3790$ K, $\log(g) = 0.8$, $[\text{Fe}/\text{H}] = -0.14$, and microturbulence = 2 km s^{-1} . The abundance results are summarized in Table 4. The CNO abundances sum up, within the uncertainties, to the solar CNO value scaled to the observed metallicity.

From synthesis of the first overtone CO, $^{12}\text{C}/^{13}\text{C} = 22 \pm 3$. The $^{12}\text{C}/^{13}\text{C}$ ratio was also computed with the curve-of-growth method (Hinkle et al. 2016). This technique yields $^{12}\text{C}/^{13}\text{C} = 30_{-16}^{+31}$, in agreement with the synthesis result. Due to rotational broadening, the spectral lines are not as deep when observed at high resolution as typically observed in an M2 III. Thus, the oxygen isotope lines could not be reliably measured.

The set of stronger CO lines in the IGR J16194–2810 spectra results in a higher abundance of $[^{12}\text{C}/\text{Fe}]$, 0.27, than the weak lines. The weak line abundance is used here. The strong CO $\Delta v=2$ lines in red giants are formed in an extended atmospheric region. This has previously been reported in single M giants by Tsuji (2008).

7. DISCUSSION

In this section the properties of the IGR J16194–2810 system defined above are discussed and compared to modeled LMXB evolution. The observed properties place IGR J16194–2810 among several other classes of objects, notably, the SyXB and the sequence E ellipsoidal variables. We will look briefly at these groups from a viewpoint of stellar evolution to see if any additional information can be gleaned on IGR J16194–2810. Finally, a model specifically tailored to IGR J16194–2810 is discussed. We conclude with brief comments on the X-ray luminosity and mass transfer.

7.1. Binary Evolution

LMXBs terminate their evolution as NS – WD binaries. The family of NS - WD binaries includes millisecond pulsars (MSP). There are currently several hundred LMXBs known (Bahramian & Degenaar 2023) and an equal number of MSP (Manchester et al. 2005; Özel & Freire 2016). LMXB evolution can be separated into two parts, (1) the formation of a binary consisting of a NS in an orbit with a low-mass star, and (2) RLO evolution resulting in a NS – WD binary (Bhattacharya & van den Heuvel 1991). We briefly review the two stages in the next subsections. IGR J16194–2810 has completed stage (1) and is in stage (2).

7.1.1. Formation of the NS – M III

The standard scenario to create a LMXB starts with a binary consisting of a primary star of mass $\gtrsim 8 M_{\odot}$ and a low mass companion. The primary evolves and expands to fill its Roche lobe. Radii of evolved massive stars are of the order several AU, larger than all but the most widely separated LMXB orbits. The existence of LMXBs requires a CE phase during which the low mass companion spirals in as the envelope of the primary is ejected (Verbunt 1993). The existence of a NS requires a SN. The CE phase reduces the mass of the primary before the SN occurs, allowing the system to stay bound (van den Heuvel & Heise 1972).

Following the CE stage, in massive stars, $M \gtrsim 12 M_{\odot}$, the star develops a degenerate iron core that exceeds the Chandrasekhar limit and collapses. NS formed from Fe-core collapse are associated with large kick velocities, typically $>200 \text{ km s}^{-1}$ (Hobbs et al. 2005). For a narrow range of primary masses, $\sim 11 M_{\odot}$, the stripped core becomes a helium star. The helium star will undergo an electron-capture supernova with minimum loss of mass and a small kick velocity (Siess & Lebreuilly 2018; Yungelson et al. 2019). In the mass range $8 - 10 M_{\odot}$, the star undergoes an AGB stage and terminates its nuclear burning lifetime as an oxygen-neon white dwarf (ONe WD) of high mass (Podsiadlowski et al. 2004; Limongi et al. 2024; Smartt 2009). The massive WD accretes mass as the companion star undergoes RLO and then undergoes accretion induced collapse (AIC), to produce the NS (Kalogera & Webbink 1998). The first two processes produce a NS with an age only a few Myrs less than that of the binary system. In AIC the NS is born only when the companion evolves to fill its Roche lobe.

Using precision orbital and NS spin properties that can be derived for binaries containing a pulsar, information on the NS progenitor can be derived (Knigge et al. 2011). However, deriving similar information on the NS progenitor in LMXBs that do not contain a pulsar is not possible. The orbits are known to much lower precision and the time since the SN has erased information even in the most favorable cases. For example, models (Section 7.3) show that the elapse time between an AIC event and the start of the RLO is $\gtrsim 10^5$ yrs. In the case of IGR J16194–2810 there

is no associated cataloged remnant and the field of IGR J16194–2810, examined in near-infrared and visual images¹⁰ shows no conspicuous nebulosity.

Similarly, as a result of a SN explosion, the resulting NS and, if present, binary companion(s), will have a kick velocity relative to the field stars. The rotation of the immediate SN progenitor (Pfahl et al 2002), the nature of the SN, the details of the pre-SN binary orbit, and the symmetry of the SN explosion all play a role in setting the kick velocity (Suárez-Andrés et al. 2015; Stevenson et al. 2022). A notable feature of IGR J16194–2810 is that its space velocity, -57.7 km s^{-1} , is similar to that of other stars in that region of the Milky Way, i.e. IGR J16194–2810 has a low kick velocity. Other long period LMXBs are known with low kick velocities (Hinkle et al. 2019, 2020) but since multiple factors determine the kick, this, like the absence of a remnant, does not provide information on the progenitor of an individual NS.

The M giant in IGR J16194–2810 was shown to have very slightly metal poor abundances with no unusual abundances in Fe, C, N, or O that could be attributable to unusual evolution or near presence to a SN. The abundances, $[\text{C}/\text{Fe}] = -0.19 \pm 0.11$, $[\text{N}/\text{Fe}] = 0.31 \pm 0.11$, and $[\text{O}/\text{Fe}] = 0.14 \pm 0.13$, are typical for field first ascent giants (Lambert & Ries 1981; Smith & Lambert 1985). These values, as well as $^{12}\text{C}/^{13}\text{C} = 22 \pm 3$, are all in agreement with material processed in the stellar interior that is being mixed to the surface during the first dredge up with standard mixing (Halabi & Eid 2015). The $[\text{Fe}/\text{H}] = -0.14 \pm 0.12$, similarly, is a typical value for a field giant (Anders et al. 2014).

The pre-SN CE event that ejects the massive star envelope does not lead to significant mass loss from the low mass star (Wang et al. 2022). The amount of ejecta captured by a companion, Δm , resulting from the SN can be estimated as

$$\Delta m \sim \Delta M_1 \left(\frac{R_2^2}{4a_o^2} \right) f$$

where ΔM_1 is the mass lost from the massive star at the time of the SN, R_2 the radius of the companion, a_o the semimajor axis at the time of the SN explosion, and f is an efficiency factor (Suárez-Andrés et al. 2015). Assuming $f = 1$, for IGR J16194–2810 the mass of ejecta captured will be on the order of 0.01% of the total SN ejecta. The current mass of the M III envelope can be estimated from the mass of the M III (Table 3) of $0.84 - 0.98 M_\odot$ less the core mass of ~ 0.35 , i.e. $\sim 0.5 - 0.6 M_\odot$. At the time of the first dredge up the envelope mass was likely $\sim 1 M_\odot$. Even in the event that the SN ejecta is several solar masses, the ejecta impacting the low mass companion is small compared to the mass of the stellar envelope. The envelope is convective and this material is mixed and ultimately makes no measurable difference in the abundances. For other SyXB systems discussed in this series of papers (Hinkle et al. 2006, 2019, 2020), no abundance peculiarities have been measured. Among shorter period LMXBs there are systems with detectable abundance abnormalities related to the SN (González Hernández et al. 2005; Suárez-Andrés et al. 2015), however, these stars are in much closer orbits and do not have convective envelopes.

7.1.2. Ellipsoidal Evolution

The nuclear evolution of a red giant core is independent of conditions in the convective envelope (Wood & Faulkner 1986). Once a star of increasing luminosity fills its Roche lobe, the transfer of the stellar envelope of the donor star continues as long as the luminosity of the donor increases. From the relations given in Section 5.2, it follows that the final binary orbital period, P_b , in days is

$$P_b \sim 1.3 \left(\frac{M_{fc}}{0.16} \right)^7$$

(Phinney & Kulkarni 1994) where the final core mass M_{fc} is in solar masses. The final core mass for IGR J16194–2810 will clearly be larger than the current core mass, so $\gtrsim 0.35$ (Section 5.2). Thus, P_b will be $\gtrsim 310$ days with considerable uncertainty due to the 7th power of the core mass. Smedley et al. (2014) provides an exponential expression that results in a similar period but, again, with very large uncertainty due to the uncertainty in the core mass.

Evolutionary tracks of LMXBs computed by Tauris & Savonije (1999) include some with roughly similar parameters to the IGR J16194–2810 system. Among these is a simulation with an M III of initial mass $1 M_\odot$, $L = 368 L_\odot$, $M_c = 0.336 M_\odot$, initial orbital period of 60 days, and a $1.3 M_\odot$ NS. While a factor of two less luminous than IGR J16194–2810 with a slightly lower core mass and shorter orbital period, this model is representative of the family

¹⁰ <http://cdsportal.u-strasbg.fr/> The Two Micron All Sky Survey (2MASS) K image shows diffuse emission extending approximately 2 arcminutes north and west. However, this is not seen in any other images, including AllWISE.

of longer orbital period NS - M III binaries. The model has a mass transfer period of 13 Myr with an initial mass-transfer rate to the NS of ~ 6 times the Eddington accretion rate, which drops to about twice the Eddington rate at the end of the mass transfer phase. The Eddington accretion rate of a $1.3 M_{\odot}$ NS for hydrogen-rich matter is $\sim 1 \times 10^{-8} M_{\odot} \text{ yr}^{-1}$ (Tauris et al. 2012). The NS accretes $0.20 M_{\odot}$ over the 13 Myr mass transfer period. A similar simulation by Podsiadlowski et al. (2002) for an initial $1 M_{\odot}$ giant with a $0.341 M_{\odot}$ core results in a $0.43 M_{\odot}$ He WD in a 617 day orbit. The initial and final NS mass were $1.4 M_{\odot}$ and $1.48 M_{\odot}$. While the average mass transfer rate is similar, a much larger peak rate is indicated with a shorter total duration of the mass transfer period, 4.5 Myr.

The IGR J16194–2810 M III has a core mass of $\sim 0.35 M_{\odot}$ and a total mass of $0.84 - 0.98 M_{\odot}$, so the envelope mass of IGR J16194–2810 is currently about 60% of the total donor mass. A typical value for similar systems at the start of RLO is 70% (Tauris & van den Heuvel 2006). This implies that the IGR J16194–2810 mass-transfer period is near the beginning with the NS mass near its original value. Masses measured for the NS in binary NS – He WD systems are $\sim 1.5 - 1.6 M_{\odot}$ (Section 4.4) and obviously include the accreted mass. This suggests a current NS mass near $1.3 M_{\odot}$.

7.2. Comparisons

IGR J16194–2810 has variously been classified as an ellipsoidal binary, a SyXB, and a LMXB. LMXBs are progenitors of NS – He WD. Here we compare IGR J16194–2810 to these groups.

7.2.1. Ellipsoidal Variables

Kiraga (2012) found IGR J16194–2810 to be an ellipsoidal variable red giant. Ellipsoidal red giant binaries consist of a Roche lobe filling red giant with a typically unseen companion (Nicholls & Wood 2012; Pawlak et al. 2014; Nie et al. 2017). The Roche lobe has a roughly ellipsoidal shape that results in brightness variations as the star rotates in the line of sight over the course of the orbit. Zahn (1977) found that stellar rotation synchronizes with orbital period on time scales much shorter than the stellar evolution time scale. In ellipsoidal variables, the Roche lobe rotates synchronously with the orbital period (Morris 1985). As a result, ellipsoidal variables form a period-luminosity sequence (‘sequence E’ Wood et al. 1999). In the case of IGR J16194–2810 the ellipsoidal period and I band magnitude, place it among the low mass stars on the ellipsoidal variable period-luminosity diagram (Figure 8).

In LMXBs the unseen companion is a NS while in field sequence E variables it is typically a main sequence star (Nie et al. 2017). Thus the mass ratio for the LMXB is reversed from sequence E variables, with the evolving star the less massive of the two. While the companion in LMXB systems is not visually bright, it is hot and X-ray luminous. The optical light curve has a bright spot resulting from heating of the M III by the NS X-ray flux. However, as in the case of IGR J16194–2810, light curve survey data is generally too noisy to reveal subtleties.

The lifetimes of MS – red giant ellipsoidal systems are less than 1 Myr, terminating when the red giant starts to overfill its Roche lobe resulting in a CE phase (Nie et al. 2012). For low mass NS systems there is a similar rapid increase of mass exchange during the first Myr. However, NS binaries are dynamically stable and super Eddington accretion onto the NS does not result in a CE phase (Tauris & Savonije 1999). As a result, lifetimes of NS – ellipsoidal variables are much longer and limited by the mass exchange rate, the mass of the donor envelope, and the donor evolutionary status (Section 7.3).

7.2.2. SySt/SyXB

IGR J16194–2810 is included on lists of SyXBs (Yungelson et al. 2019). However, most SyXBs are not Roche lobe filling. A typical system has an orbital period of years with the accretion onto the NS from the late-type giant/AGB wind (Hinkle et al. 2016). These are systems with multi-year orbital periods so that a RLO phase, if it occurs, will occur on the AGB.

There are SySt with similar orbital periods to that of IGR J16194–2810. The shortest known orbital period for a well documented SySt is for the WD+M4.5 III system T CrB with a period of 227.5 days (Fekel et al. 2000). T CrB is an ellipsoidal variable and a recurrent nova (Kraft 1958; Belczyński & Mikołajewska 1998). The more massive member of the T CrB binary is a WD near the Chandrasekhar limit (Selvelli et al. 1992). A possibly shorter period system is DASCH J075731.1+201735, an ellipsoidal M0 III with a possible WD companion, in a 119 day orbital period (Tang et al. 2012). Members of the SySt and SyXB classes are based on common observational characteristics but can have very different evolutionary paths. While both T CrB and DASCH J075731.1+201735 are RLO systems, their evolutionary path is quite different and they provide little additional insight into NS systems.

7.2.3. LMXB

The majority of LMXBs have orbital periods of days. From Kepler’s third law, the corresponding semi-major axis is on the order of 0.04 AU, roughly $10 R_{\odot}$, requiring a dwarf companion. For orbital periods of a week the semi-major axis is near 0.1 AU, implying an evolved secondary. In all LMXB the donor star is Roche lobe filling with the brightest LMXBs having observed ellipsoidal variability. For example, the $V=14.7$ system Cyg X-2 is an ellipsoidal variable with a 9.8 day orbital period, a mass function of $0.69 \pm 0.03 M_{\odot}$, and mass ratio $q = 0.34 \pm 0.04$ with a A9III donor (Casares et al. 1998). Orosz & Kuulkers (1999) found the mass of the NS to be $1.78 \pm 0.23 M_{\odot}$ and the mass of the secondary star to be $0.60 \pm 0.13 M_{\odot}$, implying that the mass transfer is well advanced.

Less well known giant LMXB systems include V395 Car = 2S 0921–630 with an orbital period of 9.0 days and accretion disk eclipses. The NS mass is $1.44 \pm 0.10 M_{\odot}$ with a companion mass of $0.35 \pm 0.03 M_{\odot}$ (Ashcraft et al. 2012). The secondary has been identified as a low luminosity K0 III of $\sim 50 L_{\odot}$ (Shahbaz et al. 1999). The semi-major axis of the 2S 0921–630 donor is 0.1 AU. This matches the radius of an early K giant, but an early K giant will be four times more luminous, placing the late-type star near the base of the giant branch. A yet more evolved system is GRO J1744–28 (Rappaport & Joss 1997). In this 11.8 day orbital period system, the envelope of the progenitor solar mass G/K III has been almost entirely stripped leaving the donor with a mass $< 0.3 M_{\odot}$ (Gosling et al. 2007).

The LMXB systems with the longest orbital periods, excluding IGR J16194–2810, are GX 13+1 and GRS 1915+05 (Bahramian & Degenaar 2023). GX 13+1 has an orbital period of 24.7 days and a K5III donor (Bandyopadhyay et al. 1999). GRS 1915+105 has an orbital period 33.9 days (Steehgs et al. 2013) with a K III donor (Greiner et al. 2001). However, this system hosts a BH primary.

The period distribution of LMXBs reflects the evolutionary time scale. Short orbital period LMXBs contain a Roche lobe filling dwarf and require an evolutionary time scale of Gyr for the core to be stripped. For system containing a red giant this takes multiple Myr. As a result the number of LMXBs is heavily skewed to short orbital periods and it is not surprising that few are known with longer periods.

7.2.4. NS – WD Binaries and Recycled Pulsars

For approximately half of the binary pulsars, the mass of the secondary requires a He WD (Phinney & Kulkarni 1994). Modeling and observations of both the MSP and LMXB groups have secured the link between these groups (Smedley et al. 2017). Mass transfer during the RLO spins up the NS and re-activates the pulsar (Phinney & Kulkarni 1994). About one-fifth of LMXBs have been found to be accreting millisecond X-ray pulsars. On the completion of the mass transfer these systems will turn into millisecond radio pulsars (Bahramian & Degenaar 2023). Models by Smedley et al. (2014, 2017) show that millisecond pulsars result from systems with initial donor masses in the range $0.875 - 1.20 M_{\odot}$ with the pulsar spin period depending on the details of the mass accretion onto the NS during RLO.

Figure 9 shows the orbital period as a function of the core mass for the NS – He WD systems with well established masses (Gao & Li 2023). A relation between period and WD mass can be established by modeling systems (Lin et al. 2011), and this is also shown. The current period and core mass of IGR J16194–2810 are shown. Since hydrogen shell burning during RLO increases the M III core mass, the core-mass orbital-period relation requires the future IGR J16194–2810 NS – WD system to have a longer period than the current orbital period of 192.5 days (Section 7.1.2).

Table 5 provides a list from the ATNF Pulsar Catalog of NS – He WD pulsars with orbital periods longer than 200 days. IGR J16194–2810, at the long orbital period end of the LMXBs, clearly represents an unusual but not unique evolutionary path. Conclusions about the fate of IGR J16194–2810 can be drawn by looking at the known NS – WD systems. Table 5 contains no fully recycled pulsars, i.e. pulsars with spin periods less than 10 ms. Four systems contain a mildly (or close to mildly) recycled pulsar with spin periods $\lesssim 35$ ms. Three systems, J0823+0159, J1803–2712, and J1822–0848, have spin periods > 300 ms. Long orbital period systems like IGR J16194–2810 are clearly not MSP progenitors. The absence in Table 5 of NS – He WD pulsars with orbital periods longer than 1000 days suggests that IGR J16194–2810 is at the long end of LMXB orbital periods for systems that can become NS – He WD pulsars. There are very few long orbital period pulsars of any type. One NS – CO/ONeMg WD pulsar, J0823+0159, has an orbital period longer than 1000 days.

7.3. FuNS Models for IGR J16194-2810

In order to more fully investigate the evolution of IGR J16194–2810 both as a current LMXB and as the progenitor of a future NS – WD binary, FuNS¹¹ code was configured for standard interacting binary evolution. The FuNS calculation is very similar to previous binary evolution calculations for the progenitors of millisecond pulsars with long orbital periods, such as those reported by [Tauris et al. \(2013\)](#) and [Wang et al. \(2022\)](#). In particular, the calculation starts with a system consisting of a main sequence star (M2) and a massive (ONe) white dwarf (M1). If the initial separation is large enough, the secondary will fill the Roche lobe when it evolves on the red giant phase. For the Roche lobe filling giant, the rate of mass-transfer through the internal Lagrangian point (L1) is calculated according to [Eggleton \(2006\)](#). At the onset of RLO, the mass-loss rate suddenly increase up to a few time $10^{-6} M_{\odot} \text{ yr}^{-1}$ (Figure 10). The amount of mass actually accreted onto the WD is calculated by following the prescriptions of [Kato & Hachisu \(2004\)](#). Since the total angular momentum is not conserved, due to mass lost by the system and emission of gravitational waves, variations of orbital separation and period must be taken into account ([de Loore & Doom 1992](#)). Note, in particular, that according to a standard assumption, the fraction of the transferred mass, M_{trans} , that is not accreted onto the compact companion, $\Delta M_{lost} = M_{trans} - M_{acc}$, is instantaneously lost by the system and that this mass removes from the system an amount of angular momentum equal to $J_{lost} = \Delta M_{lost} J_1$, where J_1 is the specific angular momentum of the WD or NS.

When the mass of the primary attains $1.38 M_{\odot}$, we assume that the WD undergoes an induced collapse that leads to the formation of a neutron star. This occurrence causes a sudden loss of gravitational binding energy, so that the resulting neutron star mass is reduced to $\sim 1.25 M_{\odot}$ (see, e.g., [Tauris et al. 2013](#)). As a consequence, the orbital separation suddenly increases and the system becomes temporarily detached. We neglect the possible effect of a kick received by the newborn NS. Later, the donor might fill the Roche lobe again initiating a second mass-transfer phase. Now, the mass-loss rate is slower and comparable to, or lower than, the shell-H burning rate, so that the core mass and luminosity of the donor can possibly increase (Figure 10). The rate of the NS accretion is calculated as the minimum between the mass transfer rate and the Eddington accretion limit, multiplied by a scaling factor representing a sort of accretion efficiency. As discussed in, e.g. [Tauris et al. \(2013\)](#), there is increasing evidence of inefficient accretion in LMXBs. As in [Wang et al. \(2022\)](#), we tentatively assume a scaling factor for the NS accretion rate of 0.3.

In order to test the code, we repeated some of the calculations discussed in [Wang et al. \(2022\)](#) and we found a reasonable agreement. In spite of this concordance, there are several uncertainties in the theoretical description of the mass transfer process that affect the quantitative result. These uncertainties concern, in particular, the recipes used to calculate the mass transfer rate, i.e. the mass lost by the RGB star during RLO, the accretion rate onto the compact companion, and the amount of mass and angular momentum effectively lost by the binary system.

To reconstruct the evolution of a system that reproduces the present-day observations, we have first selected the most likely area in the the initial parameter space. The hypothesis is that the system is in a transient phase, when the companion of the NS is evolving on the RGB. The giant is transferring mass to the compact companion. Hence, the model must fit five observational constraints, C1 – C5. The present luminosity of the RGB star is rather high, nearly $600 L_{\odot}$ (C1), not too far from the RGB tip, a fact that implies a large initial separation. This is confirmed by the large present-day orbital period, 192.5 days (C2). The present-day mass, $\sim 1 M_{\odot}$, is still high compared to its core mass, $0.35 M_{\odot}$ according to the core mass-luminosity relation. Hence, a large fraction of the envelope has not yet been lost, which implies that a short time has elapsed since RLO was initiated, no more than 10^5 yr (C3).

The initial configuration of the models is a main-sequence star, with mass between 1.2 and $1.7 M_{\odot}$ (M_2) and an ONe WD with mass between 1.2 and $1.3 M_{\odot}$ (M_1). Then, M_2 evolves into a red giant until it fills its Roche-Lobe (RL). The M_2 luminosity at the beginning of the mass transfer phase depends on the initial period (P_i) and, since the mass loss is so fast, it practically does not change until the core collapse that creates the NS. In practice, during this first mass transfer episode, the star progressively moves toward lower effective temperature and larger radii, while its luminosity does not change. In any case, the M_2 luminosity at the time of the AIC should be lower than the present-day luminosity, that is: $\log L_{AIC}/L_{\odot} < 2.8$ (C4). The mass of the RGB star immediately after the AIC depends on the initial M_1 and M_2 masses, but it is practically independent of the initial period (i.e. separation). In any case, it cannot be lower than the estimated present-day mass, namely M_2 (post AIC) $\gtrsim 1 M_{\odot}$ (C5). After the AIC the system remains detached for a short time. As the luminosity increases, the RGB star expands and fills the Roche lobe for the second time. At this stage the transfer rate is a few $10^{-7} M_{\odot} \text{ yr}^{-1}$ and the mass transfer timescale is comparable to the shell-burning timescale, so that the star may climb the RGB. Note that during this second RLO

¹¹ FUII Network Stellar evolution code; [Straniero et al. \(2006\)](#)

phase, the NS accretion occurs under a super-Eddington regime. Meanwhile, the luminosity of the RGB companion increases, until its envelope is almost fully removed. Then, the star contracts and turns off the RGB. As a consequence, its radius becomes smaller than the RL radius resulting in a detached configuration for the binary.

The results of our calculations are summarized in Table 6 and Table 7. There are three sets of models, designated G, J, and H. The initial M_1 is $1.30 M_\odot$ for models G. It is $1.25 M_\odot$ and $1.2 M_\odot$ for models J and H, respectively.

The initial configuration of the AIC models comes from a binary system with a main sequence intermediate mass star ($\sim 9 M_\odot$) and a low mass star ($\sim 1.4 M_\odot$). After the C burning, the intermediate mass star enters a super-AGB phase and fills its RL. Taking the bolometric magnitude to be about -7 and the effective temperature about 3000 K then the super-AGB star radius is of the order of $800 R_\odot$, 3.7 AU . By assuming a similar RL radius, the separation of the binary should be of the order of $1200\text{-}1500 R_\odot$, i.e. $5.6 - 7.0 \text{ AU}$. This results in a CE and all the envelope mass of the intermediate mass star is lost, while the main-sequence companion is marginally affected. The resulting binary will be a ONe WD plus the original main sequence low-mass star with the initial configuration shown for the models in Table 6.

HR diagrams of the three sets of models, G, J, and H, are presented in Figures 11, 12, and 13, respectively. All the computed evolutionary tracks pass through the (L, T_{eff}) error box for IGR J16194-2810. In addition, the luminosity at which an orbital period $P=192$ days is attained is always within the estimated error bar.

The predicted NS mass is almost independent of the choice of the initial parameter set ($1.26 - 1.27 M_\odot$). The predicted mass of the RGB star is often smaller than the measured value. Only in a few cases is it within the uncertainties (Figure 7). In Table 7 the q values predicted at $\log L=2.76$ and $P=192$ days, are shown for the G models. At $\log L=2.76$ for seven of the ten G models the predicted q ratio is within the estimated range ($0.64 - 0.98$), while when $P=192$ days, only four models are marginally compatible with the empirical estimation (see a summary in Table 7). A match/mismatch with observations could be likely due to the many uncertainties affecting close-binary evolution models, those related to the mass-loss rate, the accretion rate, etc. It should also be noted that these models are made assuming that both the RGB star and the WD/NS companion are non-rotating. Assuming that spins and orbit are synchronized, the rotation velocity of the RGB star is of the order of 15 km s^{-1} , assuming a radius of $58 R_\odot$ and $P=192$ days. This is not a huge rotation velocity if the star is a rigid rotator. On the other hand, the spin up caused by the AIC implies a quite fast rotation for the NS. This occurrence could affect the accretion rate with possible implications for the predicted NS mass and orbital separation/period.

All the models climb the RGB up to a luminosity close to the RGB tip. The final value of M_2 , i.e. the mass of the secondary at the time of the binary system detachment, is always $\geq 0.44 M_\odot$. Therefore, the possibility cannot be excluded that for some models the secondary will ignite He during the compression phase toward the WD cooling sequence. In that case, a late He-flash will occur that may trigger an ingestion of H by the flash-driven convective zone. Hence, the final outcome may be either a He WD or a CO WD. We will explore this late evolution scenario in a forthcoming paper.

7.4. Mass Transfer and Accretion

X-ray luminosity (L_X) can be converted to a mass accretion rate by scaling by c^2 (Wiktorowicz et al. 2017). For IGR J16194-2810, L_X is $2 \times 10^{35} \text{ ergs s}^{-1}$ (Section 4.2), corresponding to an accretion rate $\approx 3 \times 10^{-12} M_\odot \text{ yr}^{-1}$. This value is order of magnitudes less than that expected for a RLO system, values close to $10^{-8} M_\odot \text{ yr}^{-1}$ are expected (Sections 7.1.2 and 7.3, Figure 10). As noted by Yungelson et al. (2019), the X-ray luminosity is similar to that expected from M III wind accretion using Reimers' mass loss and a mass transfer ratio, the mass accretion rate ratioed to the mass loss rate, of $\sim 0.4\%$, similar to values found in M giant - WD symbiotics (Skopal & Cariková 2015).

The NS spin period for IGR J16194-2810 is 4.047 hours, 14570.34 s, detected in TESS photometry (Luna 2023). The NS spin period, orbital period, and X-ray luminosity of IGR J16194-2810 fall among the wind accretion SyXB on $L_x - P_{orb}$ and the Corbet $P_{spin} - P_{orb}$ diagrams (Yungelson et al. 2019). This is in contradiction to observations that IGR J16194-2810 is a RLO LMXB as well as to models, for instance Tauris & Savonije (1999) and the FuNS models, that indicate a mass accretion rate in the super Eddington regime, typically about 0.35 of the Eddington rate, of about $1 \times 10^{-8} M_\odot \text{ yr}^{-1}$.

One possible explanation is absorption of the X-ray flux by the circum-NS accretion disk. Koljonen & Hovatta (2021) note that longer orbital periods in LMXBs translate into larger Roche lobes and larger accretion disk sizes. Koljonen & Tomsick (2020) discuss several systems with large accretion disks at high orbital inclination that have intrinsic X-ray luminosities much lower than the Eddington luminosity as a result of heavy obscuration. However,

the examples cited, including the BH LMXBs V404 Cyg and GRS 1915+105, have complex time dependent X-ray behavior, which is not seen in IGR J16194–2810. On the other hand, varying obscuration by the accretion disk could be the cause of transient detections of the IGR J16194–2810 spin period (Luna 2023).

8. CONCLUSIONS

A spectroscopic orbit has been determined for the M2 III star in the binary IGR J16194–2810. This system was previously identified as an X-ray source and as an ellipsoidal variable. The M2 III is, as expected, in synchronous rotation with the orbital period. In accord with the ellipsoidal variables, the photometric period is half of the spectroscopic period. The evolutionary track and stellar surface abundances show that IGR J16194–2810 is a luminous first ascent giant with RLO. From values of the mass function and $v \sin i$ derived from observations, the mass of the NS is shown to be in the range $1.2 - 1.5 M_{\odot}$ and the mass of the M III $0.84 - 0.98 M_{\odot}$. From the luminosity, the core mass of the M III is $0.35 \pm 0.01 M_{\odot}$. Hence, the envelope mass is large, $\sim 0.5 - 0.6 M_{\odot}$, and the system appears to be at an early stage in its evolution to become a NS – WD binary.

The models show that the M III will climb the RGB up to a luminosity close to the RGB tip. The mass transfer period will be about 5.5 Myr. The final value of current M III will be $\geq 0.44 M_{\odot}$. Some models indicate that the secondary will ignite He during the compression phase toward the WD cooling sequence. In that case, a late He-flash will occur triggering ingestion of H by the flash-driven convective zone. Hence, the WD companion to the NS could be either a He WD or a CO WD. The models predict a final orbital period of $\sim 560 - 720$ days, in agreement with the system evolving into the longest period group of NS – WD pulsar binaries. The longest period NS – WD binaries do not have MSPs, likely due to shorter mass transfer period than for lower luminosity donors.

IGR J16194–2810 is a highly unusual variable star. It is an atypical member of the class of ellipsoidal variables where most members are MS – late-type giant binaries. The characteristics of IGR J16194–2810 overlap various classes of mass exchange giant binaries, most notably the symbiotics. It is included in lists of SyXB systems but most of the other members of this class have much longer orbital periods. From both a classification and evolutionary perspective it is a RLO LMXB but, again atypical, with the longest period, by a factor of more than three, of these objects. The majority of the LMXBs are systems with a star evolving off the MS. IGR J16194–2810 is at the opposite end of the luminosity distribution. Stars that are yet more luminous can not complete the removal of the donor envelope on the giant branch and will go on to become AGB systems. The M III in IGR J16194–2810 is a relatively bright star and presents an interesting object in which to observe the LMXB process.

ACKNOWLEDGMENTS

We thank an anonymous referee for highly insightful comments made from a very different perspective on the evolution of the binary than that presented in the original draft of this paper. This resulted in significant improvement in the discussion section. We thank a second referee for a detailed review that resulted in a refinement of the input parameters. We thank Luciano Piersanti for helpful discussion about binary evolution models and Bernhard Aringer for useful discussions. NOIRLab reference librarian Sharon Hunt helped us access some much needed reference materials. SM plot, developed by Robert Lupton and Patricia Monger, was used in the production of some figures. This research was facilitated by the SIMBAD database, operated by CDS in Strasbourg, France, the VizieR catalogue access tool, CDS, Strasbourg, France (DOI: 10.26093/cds/vizieR), and the Astrophysics Data System Abstract Service, operated by the Smithsonian Astrophysical Observatory under NASA Cooperative Agreement NNX16AC86A. Spectrum synthesis was carried out using MOOG. The MOOG collaboration and grant support from the U.S. National Science Foundation are acknowledged. This work made use of data from the European Space Agency (ESA) mission Gaia (<https://www.cosmos.esa.int/gaia>), processed by the Gaia Data Processing and Analysis Consortium (DPAC). Funding for the DPAC has been provided by national institutions, in particular the institutions participating in the Gaia Multilateral Agreement. The Phoenix spectrograph, used in this research, was developed at NOAO. This work used IGRINS, developed under a collaboration between the University of Texas at Austin and the Korea Astronomy and Space Science Institute (KASI) with the financial support of the US National Science Foundation under grants AST-1229522 and AST-1702267, of the University of Texas at Austin, and of the Korean GMT Project of KASI. ZGM is partially supported by a NASA ROSES-2020 Exoplanet Research Program Grant (20-XRP20 2-0125). Astronomy at Tennessee State University was supported by the State of Tennessee through its Centers of Excellence program. KHH and RRJ thank the NOAO Office of Science and the NOIRLab RSS group for support of their research. NOIRLab is managed by the Association of Universities for Research in Astronomy (AURA) under a cooperative agreement with the National Science Foundation.

OCHID identification numbers:

FRANCIS C. FEKEL [0000-0002-9413-3896]
KENNETH H. HINKLE [0000-0002-2726-4247]
RICHARD R. JOYCE [0000-0003-0201-5241]
THOMAS LEBZELTER [0000-0002-0702-7551]
ZACHARY G. MAAS [0000-0002-0475-3662]
MATTHEW MUTERSPAUGH [0000-0001-8455-4622]
JAMES SOWELL [0000-0003-3480-0957]
OSCAR STRANIERO [0000-0002-5514-6125]

REFERENCES

- Abt, H.A., Meinel, A.B., Morgan, W.W., Tapscott, J.W. 1968, *An Atlas of Low-Dispersion Grating Stellar Spectra*, (Tucson:KPNO)
- Akras, S., Guzman-Ramirez, L., Leal-Ferreira, M.L., Ramos-Larios, G. 2019, *ApJS*, 240, 2
- Anders, F., Chiappini, C., Santiago, B.X., Rocha-Pinto, H.J., Girardi, L., et al. 2014, *A&A*, 564, A115
- Ashcraft, T.A., Hynes, R.I., Robinson, E.L. 2012, *MNRAS*, 424, 620
- Asplund, M., Grevesse, N., Sauval, A. J., Scott, P. 2009, *ARA&A*, 47, 481
- Bahramian, A. & Degenaar, N. 2023, ‘Low-Mass X-ray Binaries’ in *Handbook of X-ray and Gamma-ray Astrophysics*, Bambi, C. & Santangelo, A. (eds), (Springer, Singapore), p. 1
- Bailer-Jones, C.A.L., Rybizki, J., Fouesneau, M., Demleitner, M., Adrae, R. 2021, *AJ*, 161, 147
- Bandyopadhyay, R.M., Shahbaz, T., Charles, P.A., Naylor, T. 1999, *MNRAS*, 306, 417
- Barker, E. S., Evans, D. S., Laing, J. D. 1967, *RGOB*, 130, 355
- Bassani, L., Molina, M., Malizia, A., Stephen, J.B., Bird, A.J., et al. 2006, *ApJ*, 636, L65
- Batten, A. H., Fletcher, J. M., MacCarthy, D. G. 1989, *Publ. Dominion Astrophys. Obs.*, 17, 1
- Belczyński, K., Mikołajewska, J. 1998, *MNRAS*, 296, 77
- Bessell, M.S. & Wood, P.R. 1984, *PASP*, 96, 247
- Bhattacharya, D. & van den Heuvel, E.P.J. 1991, *Physics Reports*, 203, 1
- Bird, A. J., Barlow, E. J., Bassani, L., Bazzano, A., Bélanger, G., et al. 2006, *ApJ*, 636, 765
- Brooke, J.S.A., Bernath, P.F., Western, C.M., Sneden, C., Afşar, M., et al. 2016, *JQSRT*, 168, 142
- Brooke, J.S.A., Ram, R.S., Western, C.M., Li, G., Schwenke, D.W., et al. 2014, *ApJS*, 210, 23
- Casares J., Charles P., Kuulkers E., 1998, *ApJ*, 493, L39
- de Loore, C.W.H. & Doom, C. 1992, *Structure and evolution of single and binary stars*, (Dordrecht: Kluwer Academic Publishers), *Astrophysics and Space Science Library*, Volume 179
- Dyck, H.M., Benson, J.A., van Belle, G.T., Ridgway, S.T. 1996, *AJ*, 111, 1705
- Eaton, J. A., Williamson, M. H. 2004, *Proc. SPIE*, 5496, 710
- Eaton, J. A., Williamson, M. H. 2007, *PASP*, 119, 886
- Eggleton, P. 2006, *Evolutionary Processes in Binary and Multiple Stars*, (Cambridge:Cambridge Univ. Press)
- Enoto, T., Sasano, M., Yamada, S., Tamagawa, T., Makishima, K. et al. 2014, *ApJ*, 786, 127
- Escorza, A., Siess, L., Van Winckel, H., Jorissen, A. 2020, *A&A*, 639, A24
- Fekel, F.C., Griffin, R.F. 2011, *Obs*, 131, 283
- Fekel, F.C., Joyce, R.R., Hinkle, K.H., Skrutskie, M.F. 2000, *AJ*, 119, 1375
- Fekel, F.C., Rajabi, S., Muterspaugh, M.W., Williamson, M.W. 2013, *AJ*, 145, 111
- Fekel, F.C., Tomkin, J., Williamson, M.H. 2009, *AJ*, 137, 3900
- Fitzpatrick, M.J. 1993, in *ASP Conf. Ser. 52, Astronomical Data Analysis Software and Systems II*, ed. R.J. Hanisch, R.V.J. Brissenden, & J. Barnes (San Francisco: ASP), 472
- Gaia Collaboration 2022, *VizieR Online Data Catalog*, I/350
- Gao, S.-J., Li, X.-D. 2023, *MNRAS*, 525, 2605
- González Hernández, J.I., Rebolo, R., Israelian, G., et al. 2005, *ApJ*, 630, 495
- Gosling, A. J., Bandyopadhyay, R. M., Miller-Jones, J. C. A., Farrell, S. A. 2007, *MNRAS*, 380, 1511
- Green, G.M., Schlafly, E., Finkbeiner, D., et al. 2018, *MNRAS*, 478, 651
- Green, G.M., Schlafly, E., Zucker, C. et al. 2019, *ApJ*, 887, 93
- Greiner, J., Cuby, J. G., McCaughrean, M. J., Castro-Tirado, A. J., Mennickent, R. E. 2001, *A&A*, 373, L37
- Gustafsson, B., Edvardsson, B., Eriksson, K., Jørgensen, U.G., Nordlund, Å., et al. 2008, *A&A*, 486, 951
- Halabi, G.M., Eid, M.E. 2015, *MNRAS*, 451, 2957
- Henry, G.W., Fekel, F.C., Williamson, M.H. 2022, *AJ*, 153, 180
- Hinkle, K.H., Cuberly, R.W., Gaughan, N.A., Heynssens, J.B., Joyce, R.R., et al. 1998, *Pub. SPIE*, 3354, 810
- Hinkle, K.H., Fekel, F.C., Joyce, R.R., Mikołajewska, J., Gałan, C., Lebzelter, T. 2019, *ApJ*, 872, 43
- Hinkle, K.H., Fekel, F.C., Joyce, R.R., Wood, P.R., Smith, V.V., Lebzelter, T. 2006, *ApJ*, 641, 479
- Hinkle, K.H., Lebzelter, T., Fekel, F.C., Straniero, O., Joyce, R.R., et al. 2020, *ApJ*, 904, 143
- Hinkle, K.H., Lebzelter, T., Straniero, O. 2016, *ApJ*, 886, 117
- Hinkle, K.H., Wallace, L., Livingston, W. 1995, *Infrared Atlas of the Arcturus Spectrum, 0.9 – 5.3 microns* (ASP:San Francisco)
- Hobbs, G., Lorimer, D.R., Lyne, A.G., Kramer, M. 2005, *MNRAS*, 360, 974
- Houdashelt, M.L., Bell, R.A., Sweigart, A.V., Wing, R.F. 2000, *AJ*, 119, 1424

- Hui, C.Y., Wu, K., Han, Q. et al. 2018, *ApJ*, 864, 30
- Jordi, C., Gebran, M., Carrasco, J.M., de Bruijne, J., Voss, H., Fabricius, C., et al. 2010, *A&A*, 523, A48
- Joyce, R.R. 1992, *ASPC*, 23, 258
- Kalogera, V. & Webbink, R.F. 1998, *ApJ*, 493, 351
- Kato, M. & Hachisu, I. 2004, *ApJ*, 613, L129
- Kenyon, S.J., Garcia, M.R. 1986, *AJ*, 91, 125
- Kiraga, M. 2012, *AcA*, 62, 67
- Kitamura, Y., Takahashi, H., Fukazawa, Y. 2014, *PASJ*, 66, 6
- Knigge, C., Coe, M.J., Podsiadlowski, P. 2011, *Nature*, 479, 372
- Koljonen, K.I.I. & Hovatta, T. 2021, *A&A*, 647, A173
- Koljonen, K.I.I. & Tomsick, J.A. 2020, *A&A*, 639, A13
- Kraft, R.P. 1958, *ApJ*, 127, 620
- Lacy, C.H.S., Fekel, F.C. 2011, *AJ*, 142, 185
- Lambert, D.L., Ries, L. 1981, *ApJ*, 248, 228
- Li, G., Gordon, I. E., Rothman, L. S., Tan, Y., Hu, S.-M., et al. 2015, *ApJS*, 216, 15
- Limongi, M., Lorenzo, R., Chieffi, A., Nomoto, K. 2024, *ApJS*, 270, 29
- Lin J., Rappaport S., Podsiadlowski P., et. al. 2011, *ApJ*, 732, 70
- Lucy, L. B., Sweeney, M. A. 1971, *AJ*, 76, 544
- Luna, G.J.M. 2023, *A&A*, 676, L2
- Luna, G.J.M., Sokoloski, J.L., Mukai, K., Nelson, T. 2013, *A&A*, 559, A6
- Maas, Z.G., Pilachowski, C.A. 2021, *AJ*, 161, 1830
- Manchester, R. N., Hobbs, G.B., Teoh, A., Hobbs, M. 2005, *AJ*, 129, 1993
- Masetti, N., Landi, R., Pretorius, M.L., Sguera, V., Bird, A.J., et al 2007, *A&A*, 470, 331
- Merrill, P.W., Humason, M.L. 1932, *PASP*, 44, 56
- Meyer, M.R., Edwards, S., Hinkle, K.H., Strom, S.E. 1998, *ApJ*, 508, 397
- Morgan, W.W., Keenan, P.C., Kellman, E. 1943, *An atlas of stellar spectra, with an outline of spectral classification*, (Chicago: The University of Chicago Press)
- Morris, S.L. 1985, *ApJ*, 295, 143
- Munari, U. 2019, in *The Impact of Binary Stars on Stellar Evolution*, G. Beccari & M.J. Boffin eds., (Cambridge Univ. Press., Cambridge), *Cambridge Astrophysical Series*, 54, 77
- Nicholls, C.P., Wood, P.R. 2012, *MNRAS*, 421, 2616
- Nie, J.D., Wood, P.R., Nicholls, C.P. 2012, *MNRAS*, 423, 2764
- Nie, J.D., Wood, P.R., Nicholls, C.P. 2017, *ApJ*, 835, 209
- Ochsenbein F., Bauer P., Marcout J., 2000, *A&AS*, 143, 221
- Orosz, J.A., Kuulkers, E. 1999, *MNRAS*, 305, 132
- Özel, F., Freire, P. 2016, *Ann. Rev. Astr. Astrop.*, 54, 401
- Paczyński, B. 1970, *AcA*, 20, 47
- Park, C., Jaffe, D. T., Yuk, I.-S., Chun, M.-Y., Pak, S., et al. 2014, *Proc. SPIE*, 9147, 1
- Pawlak, M., Soszyński, I., Pietrukowicz, P., et al. 2014, *Acta Astr.*, 64, 293
- Pecaut, M.J., Mamajek, E.E. 2016, *MNRAS*, 461, 794
- Pfahl, E., Rappaport, S., Podsiadlowski, P., Spruit, H. 2002, *ApJ*, 574, 364
- Phinney, E.S., Kulkarni, S.R. 1994, *Ann. Rev. Astr. Astrop.*, 32, 591
- Podsiadlowski, Ph., Langer, N., Poelarends, A.J.T., Rappaport, S., Heger, A., Pfahl, E. 2004, *ApJ*, 612, 1044
- Podsiadlowski, Ph., Rappaport, S., Pfahl, E.D. 2002, *ApJ*, 565, 1107
- Pojmański, G., Maciejewski, G. 2004, *AcA*, 54, 153
- Ramírez, I., Allende Prieto, C. 2011, *ApJ*, 743, 135
- Ramírez, S.V., DePoy, D.L., Frogel, J.A., Sellgren, K., Blum, R.D. 1997, *AJ*, 113, 1411
- Rappaport, S., Joss, P.C. 1997, *ApJ*, 486, 435
- Ratti, E.M., Bassa, C.G., Torres, M.A.P., Kuiper, L., Miller-Jones, J.C.A., et al. 2010, *MNRAS*, 408, 1866
- Renzini, A., Greggio, L., Ritossa, C., Ferrario, L. 1992, *ApJ*, 400, 280
- Rieke, G.H., Lebofsky, M.J. 1985, *ApJ*, 288, 618
- Russell, H.N. 1902, *ApJ*, 15, 252
- Savonije, G.J. 1987, *Nature*, 325, 416
- Scarfe, C.D. 2010, *Obs*, 130, 214
- Schlafly, E.F., Finkbeiner, D.P. 2011, *ApJ*, 737, 103
- Selvelli, P.L., Cassatella, A., Gilmozzi, R. 1992, *ApJ*, 393, 289
- Shahbaz, T., Kuulkers, E., Charles, P.A., et al. 1999, *A&A*, 344, 101
- Shetrone, M., Bizyaev, D., Lawler, J.E., Allende Prieto, C., Johnson, J.A., et al. 2015, *ApJS*, 221, 24
- Siess, L. & Lebreuilly, U. 2081, *A&A*, 614 A99
- Skopal, A., Cariková, Z. 2015, *A&A*, 573, A8
- Smartt, S.J. 2009, *ARA&A*, 47, 63
- Smedley, S.L., Tout, C.A., Ferrario, L., Wickramasinghe, D.T. 2014, *MNRAS*, 437, 2217
- Smedley, S.L., Tout, C.A., Ferrario, L., Wickramasinghe, D.T. 2017, *MNRAS*, 464, 237
- Smith, V.V., Lambert, D.L. 1985, *ApJ*, 294, 326
- Snedden, C. 1973, *ApJ*, 184, 839
- Soszyński, I, Udalski, A., Kubiak, M., Szymański, M.K., Pietrzyński, G., et al. 2004, *AcA*, 54, 347
- Steehgs, D., McClintock, J. E., Parsons, S. G., et al. 2013, *ApJ*, 768, 185
- Stephen, J. B., Bassani, L., Malizia, A., Bazzano, A., Ubertini, P., et al. 2006, *A&A*, 445, 869
- Sterne, T. 1941, *Proc. Natl. Acad. Sci.*, 27, 168.

- Stevenson, S., Willcox, R., Vigna-Gómez, A., Broekgaarden, F. 2022, MNRAS, 513, 6105
- Straniero, O., Gallino, R., Cristallo, S. 2006, NuPhA, 777, 311
- Suárez-Andrés, L., González Hernández, J.I., Israelian, G. et al. 2015, MNRAS, 447, 2261
- Tang, S., Grindlay, J.E., Moe, M., Orosz, J.A., Kurucz, R.L., Quinn, S.N. et al. 2012, ApJ, 751, 99
- Tauris, T.M., Langer, N., Kramer, M. 2012, MNRAS, 425, 1601
- Tauris, T.M., Sanyal, D., Yoon, S.-C., Langer, N. 2013, A&A, 558, A39
- Tauris, T.M. & Savonije, G.J. 1999, A&A, 350, 928
- Tauris, T.M. & van den Heuvel, E.P.J. 2006, 'Formation and Evolution of Compact Stellar X-ray Sources' in Compact Stellar X-ray Sources, Lewin, W. & van der Klis, M. (eds), Cambridge Astrophysics Series, No. 39. (Cambridge, UK: Cambridge University Press), p. 623
- Tokunaga, A. 2000, 'Infrared Astronomy', Allen's Astrophysical Quantities, 4th edition, ed. A. N. Cox, (New York: AIP Press, Springer), p.143
- Tsuji, T. 2008, A&A, 489, 1271
- Tuchman, Y., Glasner, A., Barkat, Z. 1983, ApJ, 268, 356
- van Belle, G.T, Lane, B.F., Thompson, R.R., Boden, A.F., Colavita, M.M., et al. 1999, AJ, 117, 521
- van den Heuvel, E.P.J. & Heise, J., 1972, Nature Physical Science, 239, 67
- Verbunt, F. 1993, ARA&A, 31, 93
- Verbunt, F., van den Heuvel, E.P.J. 1995, in X-Ray Binaries, ed. W.H.G. Lewin, J. van Paradijs, E.P.J. van den Heuvel (Cambridge: Cambridge University Press), p. 457
- Wallace, L., Hinkle, K.H. 1997, ApJS, 111, 445
- Wang, B., Liu, D., Chen, H. 2022, MNRAS, 510, 6011
- Warner, B. 1995, Cataclysmic Variable Stars (Cambridge University Press:Cambridge)
- Webbink, R.F., Rappaport, S., & Savonije, G.J. 1983, ApJ, 270, 678
- Wiktorowicz, G., Sobolewska, M., Lasota, J.-P., Belczynski, K. 2017, ApJ, 846, 17
- Willmarth, D.W., Fekel, F.C., Abt, H. A., Pourbaix, D. 2016, AJ, 152, 46
- Wilsing, J. 1893 Astronomische Nachrichten, 134, 89
- Wilson, R.E., Devinney, E.J. 1971, ApJ, 166, 605
- Wolfe, R.H., Horak, H.G., Storer, N.W. 1967, in Modern Astrophysics, ed. M. Hack (New York: Gordon & Breach), 251
- Wood, P.R., Alcock, C., Allsman, R.A., et al. 1999 in IAU Symp. 191, Asymptotic Giant Branch Stars, ed. T. LeBertre, A. Lèbre, & C. Waelkens, 151
- Wood, P.R., Faulkner, D.J. 1986, ApJ, 307, 659
- Worthey, G. & Lee, H.-C. 2011, ApJS, 193, 1
- Yungelson, L.R., Kuranov, A.G., Postnov, K.A. 2019, MNRAS, 485, 851
- Zahn, J.-P. 1977, A&A, 57, 383

Table 1. Radial Velocity Observations of IGR J16194–2810

Hel. Julian Date HJD–2,400,000	Phase	RV (km s ⁻¹)	(<i>O</i> – <i>C</i>) ^{<i>a</i>} (km s ⁻¹)	Source ^{<i>b</i>}
58230.776	0.867	14.1	1.4	IGRINS
58559.916	0.577	–27.0	0.0	Phoenix
58660.726	0.100	18.0	1.7	Fair
58661.726	0.106	16.7	0.9	Fair
58981.836	0.769	–2.5	–1.1	Fair
58982.836	0.774	–1.6	–1.1	Fair
59021.726	0.976	21.7	0.8	Fair
59022.726	0.981	19.8	–1.2	Fair
59023.726	0.986	21.3	0.2	Fair
59024.726	0.992	21.8	0.6	Fair
59025.726	0.997	20.7	–0.5	Fair
59026.726	0.002	20.5	–0.7	Fair
59029.726	0.018	20.8	–0.3	Fair
59031.726	0.028	20.5	–0.3	Fair
59296.789	0.405	–25.6	–0.1	Fair
59302.984	0.437	–26.6	1.4	Fair
59303.984	0.443	–28.7	–0.4	Fair
59304.984	0.448	–28.6	0.0	Fair
59307.984	0.463	–28.6	0.7	Fair
59308.984	0.469	–28.4	1.0	Fair
59315.925	0.505	–29.8	0.1	Fair
59317.925	0.515	–30.4	–0.6	Fair
59318.925	0.520	–29.9	–0.2	Fair
59340.856	0.634	–20.5	0.9	Fair
59342.856	0.645	–20.6	–0.5	Fair
59345.856	0.660	–16.3	1.8	Fair
59346.856	0.665	–17.1	0.2	Fair
59347.856	0.671	–17.1	–0.5	Fair
59349.856	0.681	–15.4	–0.3	Fair
59350.856	0.686	–14.0	0.4	Fair
59352.856	0.697	–13.0	–0.2	Fair
59353.826	0.702	–11.8	0.2	Fair
59354.827	0.707	–12.4	–1.2	Fair
59356.827	0.717	–8.7	0.9	Fair

Table 1 continued on next page

Table 1 (*continued*)

Hel. Julian Date	Phase	RV	$(O - C)^a$	Source ^b
HJD–2,400,000		(km s ^{–1})	(km s ^{–1})	
59357.807	0.722	–9.5	–0.7	Fair
59364.797	0.759	–2.5	0.5	Fair
59365.797	0.764	–2.6	–0.4	Fair
59372.767	0.800	1.6	–1.9	Fair
59373.767	0.805	2.3	–2.0	Fair
59374.767	0.810	3.8	–1.3	Fair
59375.767	0.816	6.3	0.4	Fair
59377.756	0.826	7.0	–0.4	Fair
59392.716	0.904	17.0	0.3	Fair
59447.672	0.189	7.1	1.9	Fair
59657.983	0.282	–11.0	–1.6	Fair
59658.983	0.287	–11.1	–0.8	Fair
59663.983	0.313	–14.6	–0.4	Fair
59664.984	0.318	–15.3	–0.3	Fair
59675.984	0.375	–23.0	–0.5	Fair
59676.984	0.381	–23.1	0.0	Fair
59683.915	0.417	–26.3	0.2	Fair
59684.915	0.422	–27.3	–0.4	Fair
59690.915	0.453	–29.7	–0.9	Fair
59691.916	0.458	–29.7	–0.6	Fair
59693.916	0.469	–28.6	0.8	Fair
59694.916	0.474	–28.9	0.7	Fair
59710.836	0.556	–28.3	0.0	Fair
59711.836	0.562	–28.0	0.0	Fair
59712.836	0.567	–27.6	0.1	Fair
59714.836	0.577	–27.6	–0.6	Fair
59717.806	0.593	–25.8	–0.1	Fair
59719.807	0.603	–25.1	–0.3	Fair
59724.797	0.629	–23.2	–1.2	Fair
59730.797	0.660	–17.8	0.2	Fair
59731.797	0.665	–18.2	–0.9	Fair

^aO–C = Observed minus calculated radial velocity

^bIGRINS = IGRINS at GS, Phoenix = Phoenix at GS, Fair = Tennessee State University 2 m AST and fiber-fed echelle spectrograph at Fairborn Observatory

NOTE—This table is available in machine-readable form.

Table 2. IGR J16194–2810 Spectroscopic Orbital Elements and Related Parameters

Parameter	Value
P (days)	192.47 ± 0.13
T_0 (HJD)	2459026.33 ± 0.33
K (km s ⁻¹)	25.58 ± 0.16
γ (km s ⁻¹)	-4.36 ± 0.13
$a \sin i$ (10 ⁶ km)	67.69 ± 0.42
f(m) (M_\odot)	0.3337 ± 0.0062
S.E. ^a (km s ⁻¹)	0.9

^aStandard error of an observation of unit weight

Table 3. Parameters of the IGR J16194–2810 Giant

Parameter	Value	Source
Distance	2101 ± 150 pc	Gaia EDR3
Spectral Type	M2 III	Literature, TiO
Effective Temperature	3700 ± 100 K	Sp.Ty., photometry
Luminosity	$573^{+72}_{-79} L_{\odot}$	Distance, K_0
Radius	$58 \pm 7 R_{\odot}$	L, T_{eff}
Mass	$0.91 \pm 0.07 M_{\odot}$	Ellipsoidal, NS mass
Surface gravity ^a	$5 - 11$ cm s ⁻²	Mass and radius
Inclination	$55 - 70^{\circ}$	Ellipsoidal
Equatorial Rotation	18 ± 2 km s ⁻¹	$v \sin i$ and inclination

^a $\log(g) \sim 1$

Table 4. Abundances of the IGR J16194–2810 Giant

Element	Value	Number of lines synthesized	Species
[Fe/H]	-0.14 ± 0.12	7	Fe I
[C/Fe]	-0.19 ± 0.11	6	$^{12}\text{CO } \Delta v=2$
[N/Fe]	0.31 ± 0.11	9	CN Red $\Delta v=-1$
[O/Fe]	0.14 ± 0.13	15	OH $\Delta v=2$
$^{12}\text{C}/^{13}\text{C}$	22 ± 3	5	$^{13}\text{CO } \Delta v=2$

Table 5. Long Orbital Period Pulsars

Name	Orbital Period ^a (days)	Spin Period (milliseconds)	WD type ^b
J0214+5222	512.0	24.5	He
J0407+1607	669.1	25.7	He
J0823+0159	1232.4	864.9	CO
J1711–4322	922.5	102.6	He
J1803–2712	406.8	334.4	He
J1822–0848	286.8	834.8	He:
J1840–0643	944.6	35.6	He
J2016+1948	635.0	64.9	He:
J2204+2700	815.2	84.7	He:

^aLow mass systems with orbital periods > 200 days from ATNF Pulsar Catalog Version 1.70. Globular cluster pulsars and systems with highly uncertain secondary types are omitted.

^bColon indicates uncertain designation.

Table 6. FuNS Interacting Binary Evolution Models^a

Model Name	Initial			AIC			L _{M2} =2.76			P=192			Final				
	M ₁	M ₂	P	L ₂	M ₂	P	T _{eff}	M ₁	M ₂	P	T _{eff}	L ₂	M ₁	M ₂	M ₁	M ₂	P
G1	1.30	1.20	120.00	2.74	1.08	128.10	3.57	1.25	1.08	143.00	3.56	2.82	1.26	0.88	1.30	0.46	703.50
G2	1.30	1.30	90.00	2.65	1.17	95.36	3.56	1.27	0.82	180.00	3.56	2.77	1.27	0.79	1.31	0.44	616.70
G3	1.30	1.40	80.00	2.62	1.24	84.85	3.56	1.27	0.77	190.50	3.56	2.76	1.27	0.77	1.32	0.44	595.40
G4	1.30	1.40	90.00	2.68	1.24	95.40	3.56	1.26	0.89	165.80	3.56	2.79	1.27	0.82	1.31	0.45	643.70
G5	1.30	1.40	100.00	2.72	1.24	105.90	3.58	1.25	1.13	130.70	3.56	2.81	1.26	0.87	1.31	0.45	689.50
G6	1.30	1.50	80.00	2.65	1.30	85.61	3.56	1.27	0.81	181.00	3.56	2.77	1.27	0.79	1.32	0.44	615.30
G7	1.30	1.50	90.00	2.71	1.30	96.20	3.57	1.26	0.97	152.20	3.56	2.80	1.27	0.84	1.31	0.45	664.80
G8	1.30	1.60	70.00	2.62	1.32	77.18	3.55	1.28	0.74	199.20	3.55	2.75	1.27	0.75	1.32	0.44	577.80
G9	1.30	1.60	80.00	2.68	1.32	87.85	3.56	1.26	0.86	172.80	3.56	2.78	1.27	0.81	1.31	0.45	631.20
G10	1.30	1.70	70.00	2.64	1.27	82.84	3.55	1.27	0.77	192.20	3.55	2.76	1.27	0.77	1.32	0.44	592.40
J1	1.25	1.30	80.00	2.60	1.04	95.43	3.55	1.28	0.70	207.20	3.55	2.74	1.27	0.73	1.32	0.44	558.70
J2	1.25	1.30	90.00	2.65	1.04	107.60	3.56	1.27	0.79	185.50	3.56	2.77	1.27	0.78	1.31	0.44	604.70
J3	1.25	1.40	80.00	2.63	1.06	99.61	3.55	1.27	0.75	194.60	3.56	2.76	1.27	0.76	1.32	0.44	586.10
J4	1.25	1.40	90.00	2.68	1.06	112.20	3.56	1.26	0.86	170.70	3.56	2.78	1.27	0.81	1.31	0.45	634.00
J5	1.25	1.40	100.00	2.73	1.06	124.70	3.57	1.25	1.02	145.50	3.56	2.81	1.26	0.86	1.30	0.45	679.40
J6	1.25	1.50	80.00	2.66	1.05	106.70	3.56	1.27	0.80	184.10	3.56	2.77	1.27	0.78	1.31	0.44	608.30
J7	1.25	1.60	80.00	2.68	1.01	117.80	3.56	1.26	0.84	175.90	3.56	2.78	1.26	0.80	1.31	0.45	624.60
J8 ^b	1.25	1.60	100.00	2.78	1.01	147.90	3.56	2.83	1.26	0.91	1.30	0.46	723.50
H1	1.20	1.20	100.00	2.67	0.90	129.20	3.56	1.26	0.77	191.00	3.56	2.76	1.26	0.76	1.31	0.44	591.80
H2	1.20	1.20	120.00	2.75	0.89	156.10	3.56	1.25	0.89	175.70	3.56	2.80	1.25	0.85	1.30	0.45	667.10
H3 ^b	1.20	1.20	130.00	2.79	0.89	170.10	3.56	2.81	1.25	0.89	1.30	0.46	702.50
H4	1.20	1.40	100.00	2.73	0.92	144.70	3.56	1.25	0.92	164.20	3.56	2.80	1.26	0.83	1.30	0.45	656.00

^a Units: mass=M_⊙, period=days, luminosity=log(L/L_⊙), effective temperature=log(T_{eff})^b In models J8 and H3, the AIC occurs at log L>2.76

Table 7. Predicted q Values^a

Model Name	L=2.76			P=192		
	M_1	M_2	q	M_1	M_2	q
G1	1.25	1.08	0.86	1.26	0.88	0.70
G2	1.27	0.82	0.65	1.27	0.79	0.62
G3	1.27	0.77	0.61	1.27	0.77	0.61
G4	1.26	0.89	0.71	1.27	0.82	0.65
G5	1.25	1.13	0.90	1.26	0.87	0.69
G6	1.27	0.81	0.64	1.27	0.79	0.62
G7	1.26	0.97	0.77	1.27	0.84	0.66
G8	1.28	0.74	0.58	1.27	0.75	0.59
G9	1.26	0.86	0.68	1.27	0.81	0.64
G10	1.27	0.77	0.61	1.27	0.77	0.61

^aUnits: mass= M_\odot , period=days,
luminosity= $\log(L/L_\odot)$

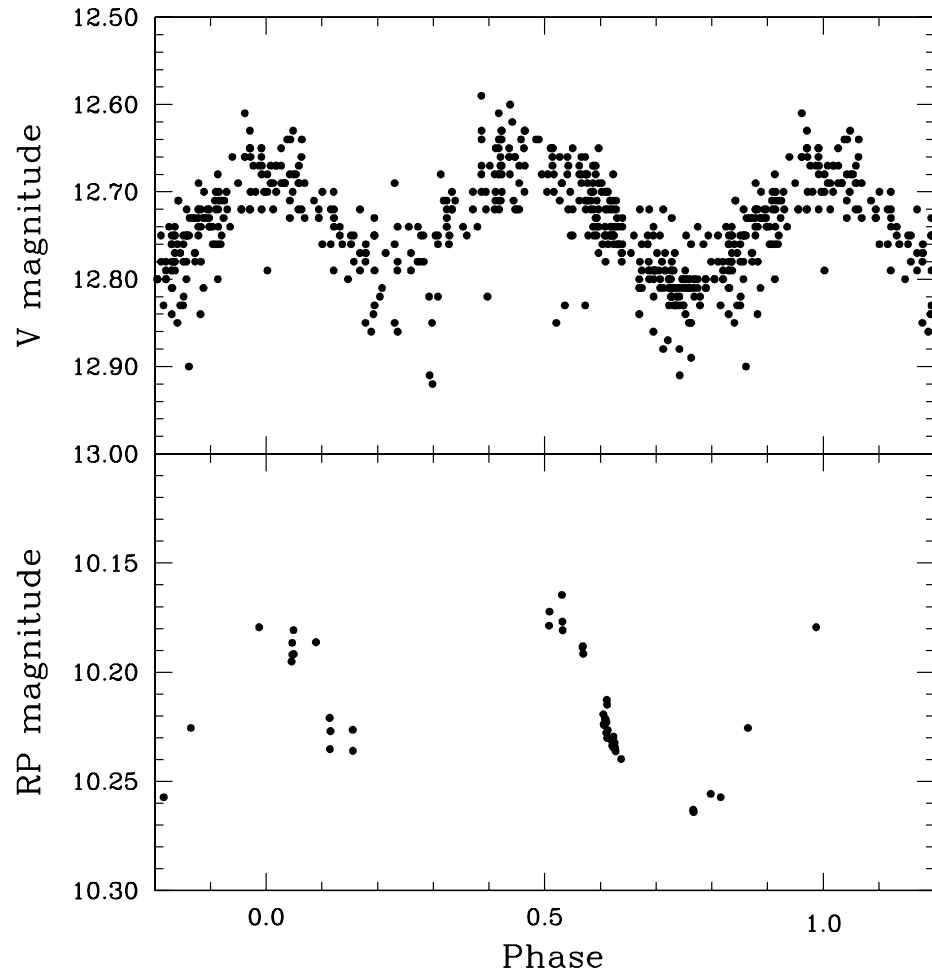


Figure 1. Top: The V band light curve of IGR J16194–2810 phased to 192.8 d from Kiraga (2012). Bottom: The Gaia RP -band light curve of IGR J16194–2810. The system is ellipsoidal and there are two maxima and minima in each orbital cycle.

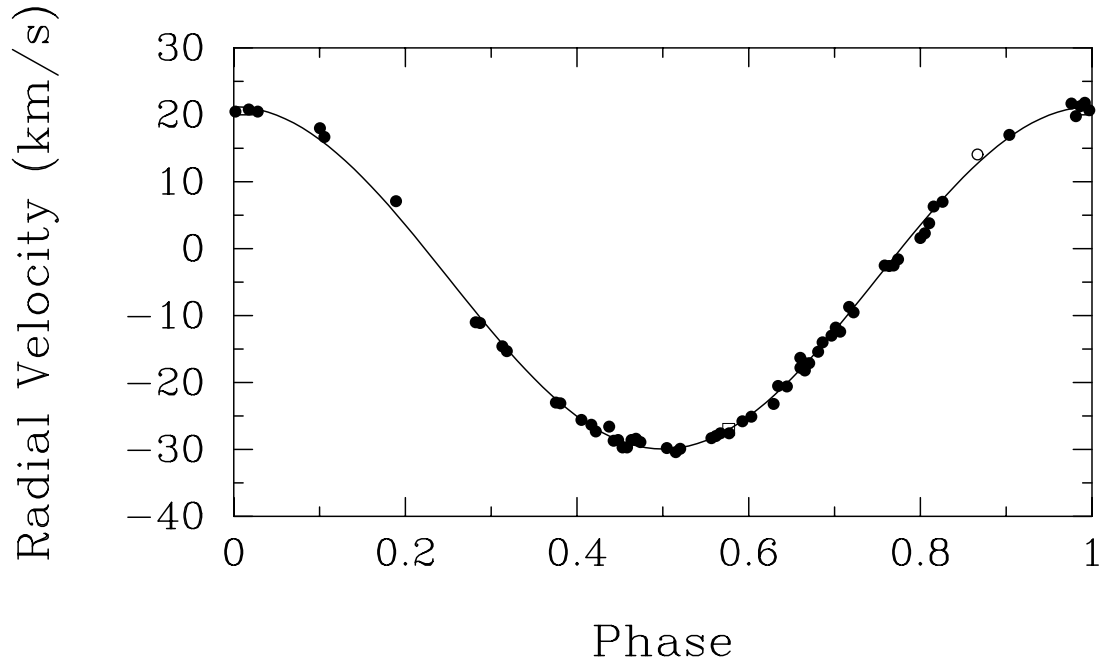


Figure 2. A plot of the IGR J16194–2810 radial velocities (Solid circles = Fairborn Observatory, open circle = IGRINS, and open box = Phoenix) compared with the computed velocity curve (solid line). The standard error of an observation is 0.9 km s^{-1} . Phase zero is a time of maximum velocity. The binary has an orbital period of 192.5 days.

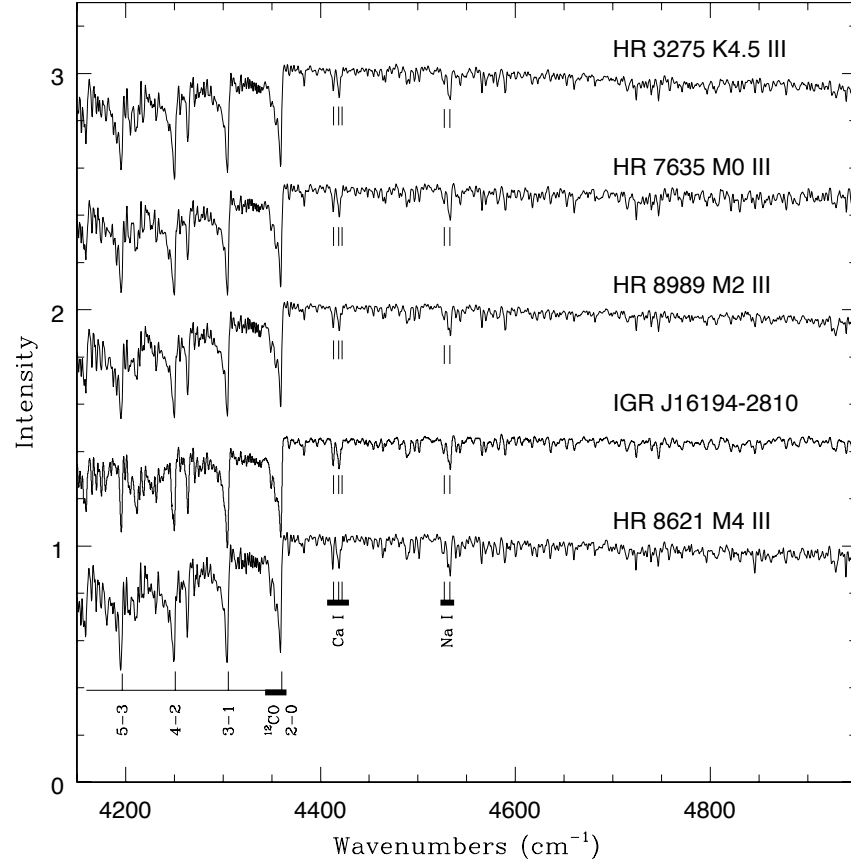


Figure 3. The IGRINS K band spectrum of IGR J16194–2810 convolved to $R=3000$ and compared to standard giant star spectra from Wallace & Hinkle (1997). The bars mark the Ramírez et al. (1997) spectral indices. The major spectral features are indicated by vertical lines.

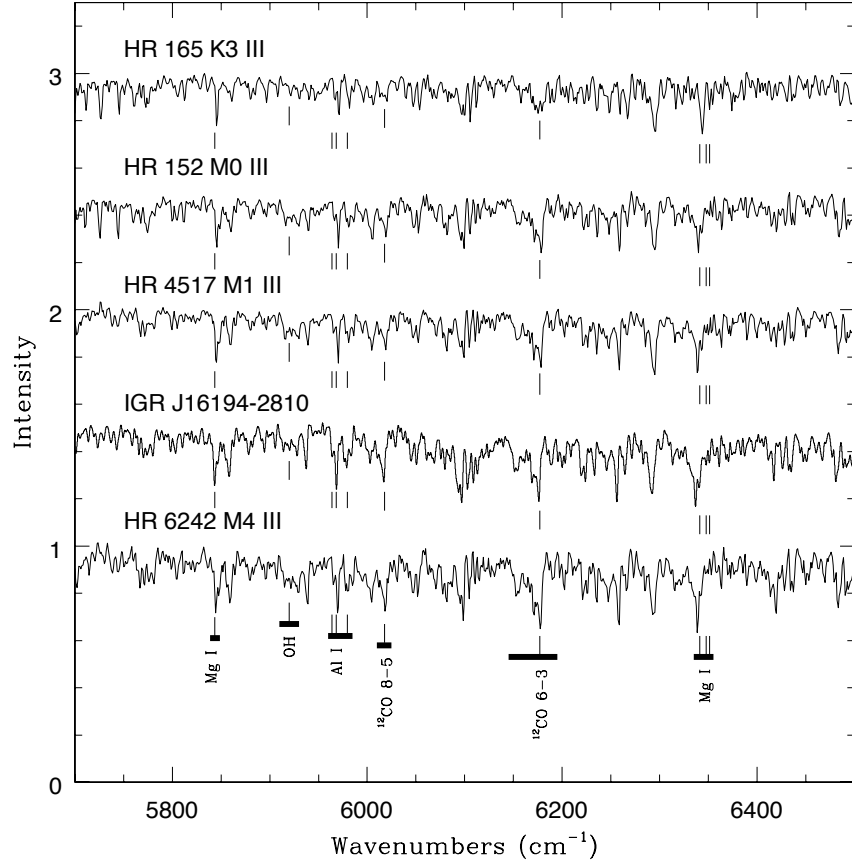


Figure 4. The IGRINS H band spectrum of IGR J16194–2810 convolved to $R=3000$ and compared to standard giant star spectra from Meyer et al. (1998). The bars mark the cool star spectral indices of Meyer et al. (1998) with the spectral features listed in Table 4 of Meyer et al. (1998) indicated by vertical lines. The increase in strength of the ^{12}CO 6-3 index with cooler spectral type is apparent in the Figure.

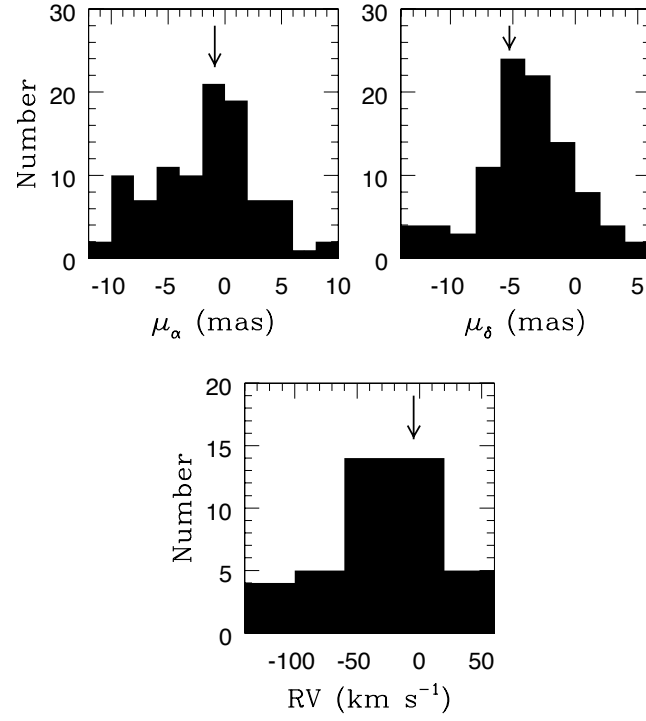


Figure 5. Histograms of Gaia DR3 proper motions and radial velocities in 20 arcmin radius around the position of IGR J16194–2810. The parallax was restricted to between 0.35 and 0.65 mas with a parallax error less than or equal 0.045 mas. The positions of the IGR J16194–2810 values are marked with the arrows.

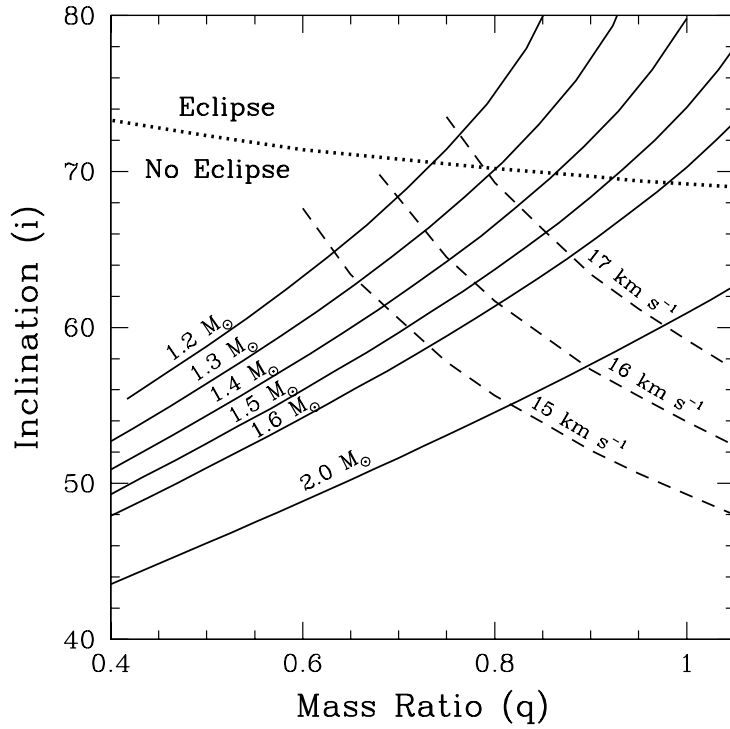


Figure 6. The inclination as a function of the mass ratio (q). The solid lines are labelled with the NS mass. The system does not eclipse, and the eclipse limit is shown by the dotted line. The dashed curves show the ellipsoidal relation between the $v \sin i$ of the M III and the mass ratio for the range of $v \sin i$ values. The intersection of the solid and dashed lines sets limits on q and i .

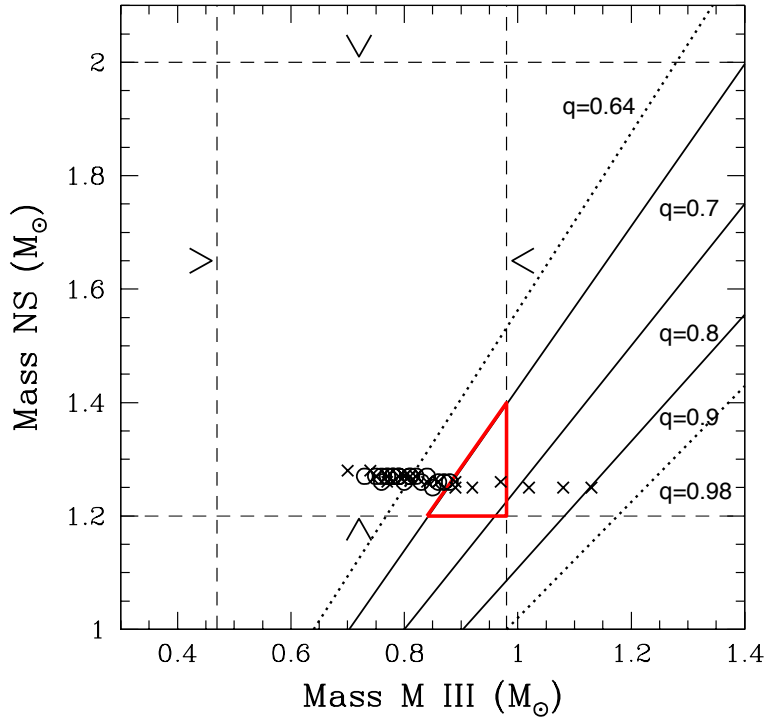


Figure 7. The range of the NS mass is shown as a function of the derived M III mass and derived values of the mass ratio q . The dashed lines and carets show the limits on the NS mass, $1.2 - 2.0 M_{\odot}$ and the M III mass $0.47 - 0.98 M_{\odot}$. The solid curves are values of q for a projected rotation velocity of 16 km s^{-1} . The dotted lines are extreme values, $q = 0.64$ and 0.98 . The masses of the two binary components fall in the triangle, NS mass $1.2 - 1.5 M_{\odot}$ and M III mass $0.75 - 0.98 M_{\odot}$ with the red triangle corresponding to more probable values of q . X symbols locate the model M_2 (M III) versus M_1 (NS) at $\log(L_2)=2.76$, open circles at orbital period 192 days.

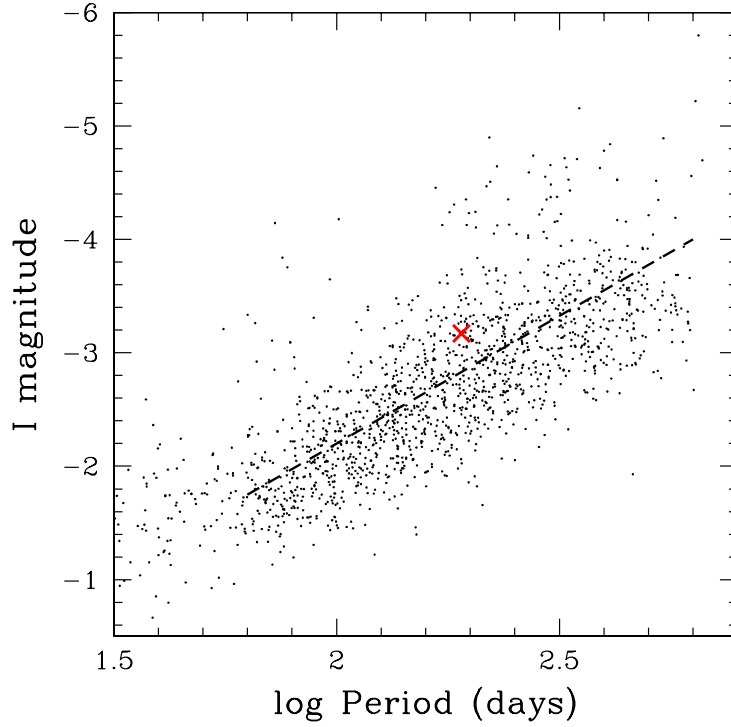


Figure 8. The Ellipsoid Period-Luminosity (P-L) diagram. The dots are ellipsoidal variables in the LMC (Soszyński et al. 2004) with an adopted distance modulus of 18.5. No de-reddening has been applied. The dashed line is the fit in the interval $1.75 < \log(P) < 2.85$ from Nie et al. (2017). Massive ellipsoidal variables are more luminous and appear at the upper edge of the P-L distribution. Systems with M giants of mass $< 1.85 M_{\odot}$ are scattered around the line (Nie et al. 2017). The red x marks the position of IGR J16194–2810 for an observed $I = 9.98$ mag and $A_I = 1.54$ mag, i.e. a de-reddened $I = 8.44$ mag. Assuming a distance to IGR J16194–2810 of 2101 pc, the absolute, de-reddened I is -3.17 mag.

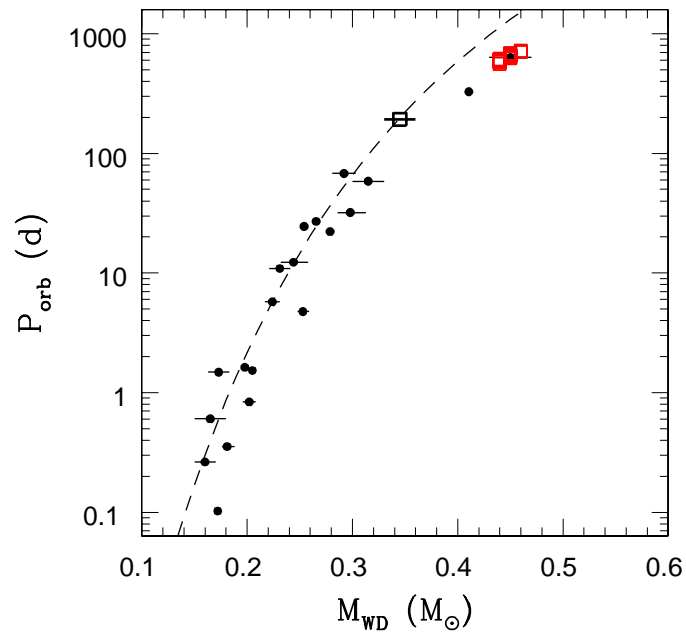


Figure 9. Orbital periods as a function of the WD masses for 20 NS – He WD systems where the uncertainties in the WD mass are no more than $0.02 M_{\odot}$ (Table 2 of Gao & Li 2023). Where the uncertainties in the mass are large enough to be plotted they are shown as a horizontal line. The dashed line is the period – white dwarf mass relation of Lin et al. (2011). The measured period and the core mass, derived from the core-mass luminosity relation, is shown for IGR J16194–2810 (open black square). Predicted values for the evolutionary end product NS – WD are taken from Table 6 and shown as open red squares.

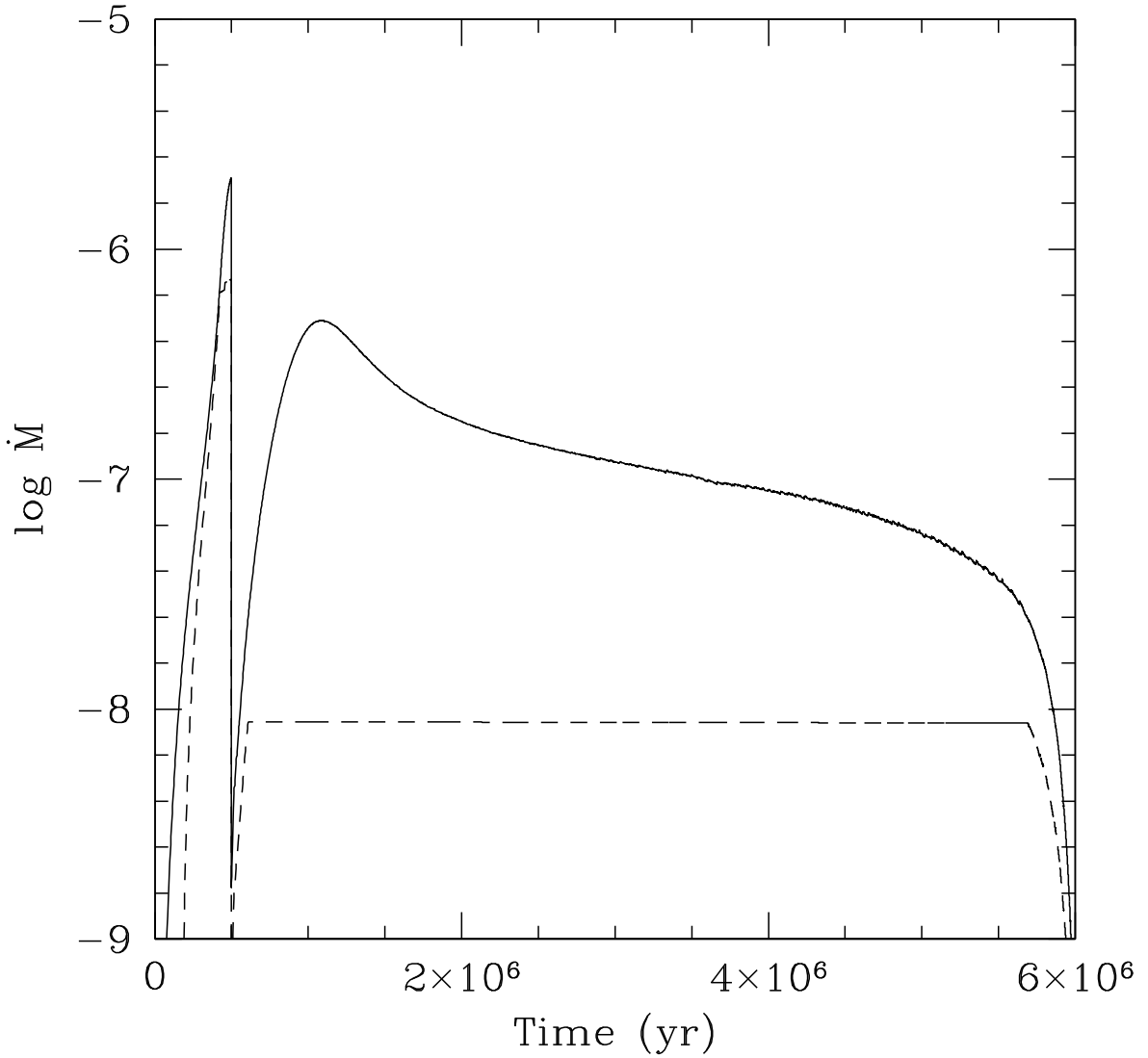


Figure 10. Mass transfer rate (solid line) and mass accretion rate onto the WD/NS (dashed line) versus time, for the model G4 (see Table 6). As described in the text, two distinct phases are recognizable. Before the AIC, once the secondary RLO occurs mass transfer and accretion to the massive WD is quite fast. After RLO of $\sim 5 \times 10^5$ yr, the white dwarf attains the Chandrasekhar limit and collapses. Then, for a short time, the system consisting of a bright giant and a neutron star remains detached, until the RGB star again fills the Roche lobe. During this second mass transfer phase, that lasts for $\sim 5 \times 10^6$ yr, only a small fraction of the mass lost by the giant star is actually accreted onto the NS surface. As a consequence of the mass and angular momentum losses, the period and the orbital separation progressively increase. The RLO ceases when the mass of the giant is reduced to $\lesssim 0.5 M_{\odot}$.

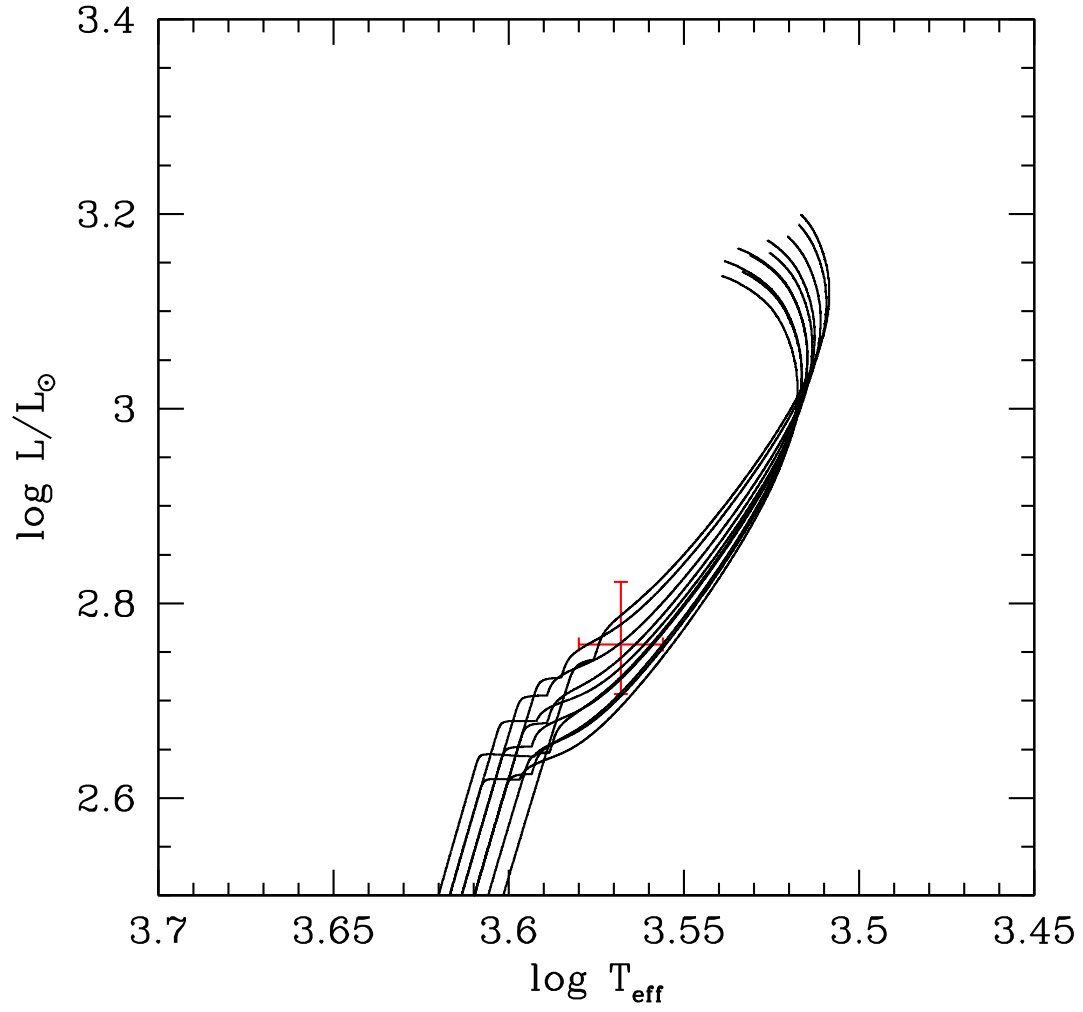


Figure 11. HR diagram of models G1 – G9 (Table 6). L - T_{eff} for IGR J16194–2810 M₂ is shown (red) with uncertainties from Table 3.

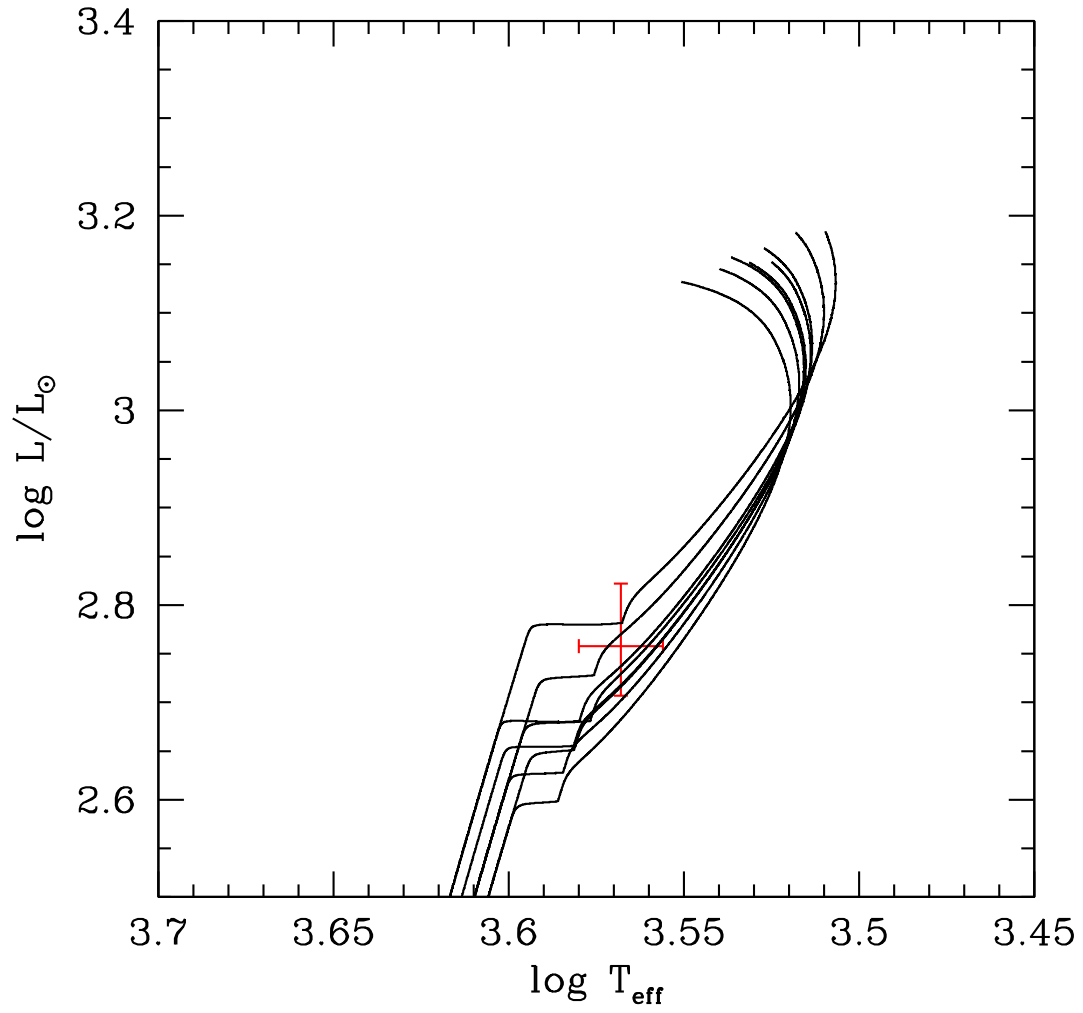


Figure 12. As in Figure 11 with models J1 – J7 shown as black lines.

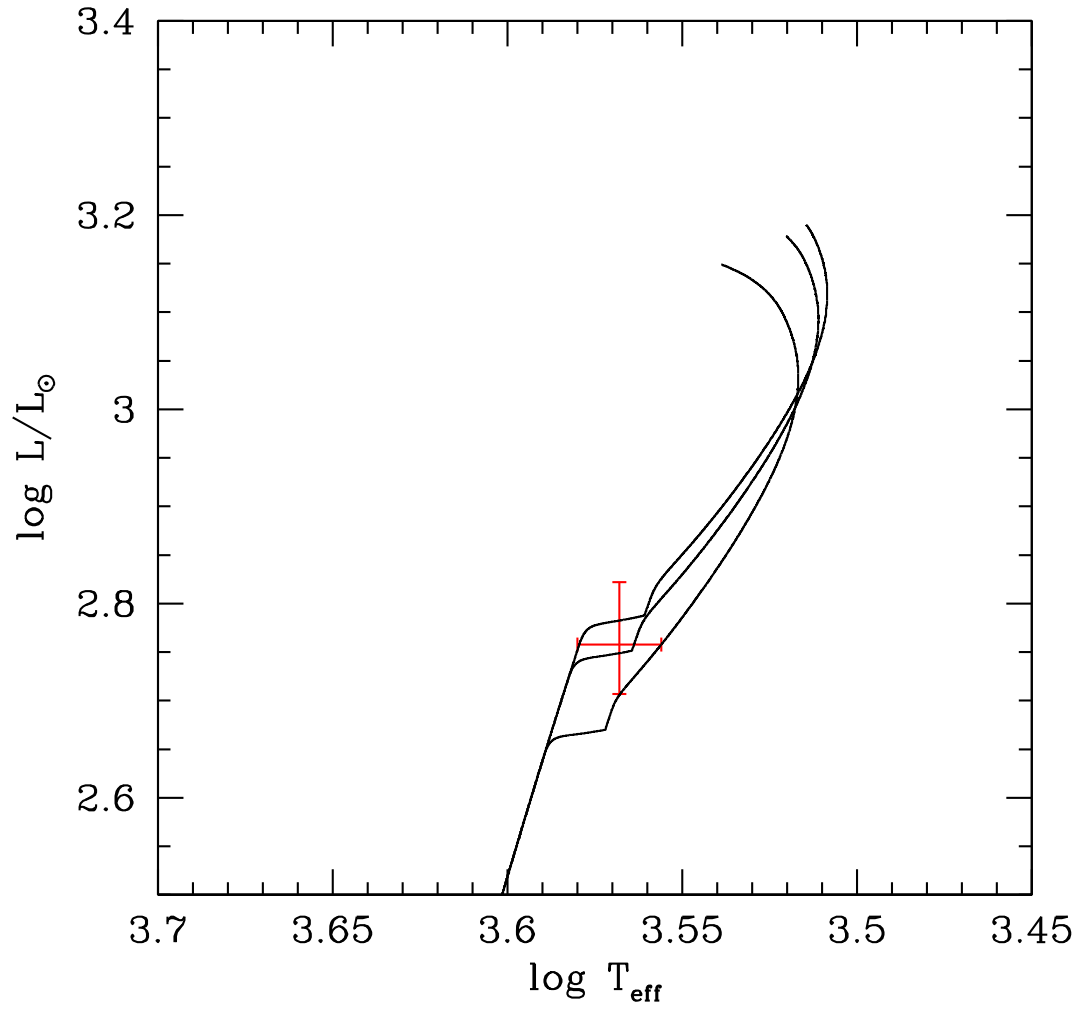


Figure 13. As in Figure 11 with models H1, H2 and H4 shown as black lines.